

Will ALMA reveal the true core mass function of protoclusters?

P. Padoan^{1,2}★, V.-M. Pelkonen¹★, M. Juvela³, T. Haugbølle⁴ and Å. Nordlund⁴

¹*Institut de Ciències del Cosmos, Universitat de Barcelona, IEEC-UB, Martí i Franqués 1, E08028 Barcelona, Spain*

²*ICREA, Pg. Lluís Companys 23, E-08010 Barcelona, Spain*

³*Department of Physics, University of Helsinki, PO Box 64, 00014, Helsinki, Finland*

⁴*Niels Bohr Institute, University of Copenhagen, Øster Voldgade 5-7, DK-1350 Copenhagen, Denmark*

Accepted 2023 April 15. Received 2023 April 3; in original form 2023 January 19

ABSTRACT

Characterizing pre-stellar cores in star-forming regions is an important step towards the validation of theoretical models of star formation. Due to their sub-arcsecond resolution, ALMA observations can potentially provide samples of pre-stellar cores up to distances of a few kpc, where regions of massive star formation can be targeted. However, the extraction of real cores from dust-continuum observations of turbulent star-forming clouds is affected by complex projection effects. In this work, we study the problem of core extraction both in the idealized case of column-density maps and in the more realistic case of synthetic 1.3 mm ALMA observations. The analysis is carried out on 12 regions of high column density from our 250 pc simulation. We find that derived core masses are highly unreliable, with only a *weak correlation* between the masses of cores selected in the synthetic ALMA maps and those of the corresponding three-dimensional cores. The fraction of real three-dimensional cores detected in the synthetic maps increases monotonically with mass and remains always below 50 per cent. Above $\sim 1 M_{\odot}$, the core mass function derived from the column-density maps is steeper than that of the three-dimensional cores, while the core mass function from the synthetic ALMA maps has a slope closer to that of the real three-dimensional cores. Because of the mass uncertainties, proper guidance from realistic simulations is essential if ALMA observations of protoclusters at kpc distances are to be used to test star formation models.

Key words: MHD – turbulence – stars: formation – stars: luminosity function, mass function.

1 INTRODUCTION

The relation between the mass of a pre-stellar core and that of the star it forms is an important prediction of theoretical models of star formation. On the one hand, in the core-collapse model (McKee & Tan 2002, 2003) and in some models of the initial mass function (IMF) of stars (e.g. Hennebelle & Chabrier 2008; Hopkins 2012), it is assumed that the stellar mass reservoir is fully contained in a bound pre-stellar core. On the other hand, in the competitive accretion model (Zinnecker 1982; Bonnell et al. 2001a, b), most of the stellar mass is accreted over time from a larger gas reservoir shared with other stars, with an accretion rate that depends on the mass of the star. Numerical simulations of star formation under turbulent conditions consistent with Larson’s velocity–size relation (e.g. Larson 1981; Heyer & Brunt 2004) and with virial parameter of order unity seem to rule out both models (Padoan, Haugbølle & Nordlund 2014; Pelkonen et al. 2021) and to suggest an alternative scenario, the *inertial-inflow model*, where the pre-stellar core contains only a fraction of the final stellar mass, while the remaining mass is brought to the star from larger scale by pre-existing converging flows (Padoan et al. 2020; Pelkonen et al. 2021). The IMF model of Padoan & Nordlund (2002) is consistent with this alternative scenario, as the final stellar mass is determined by pre-existing converging flows, and can be

much larger than the critical mass, particularly towards larger stellar masses (Padoan & Nordlund 2011).

Observations do not directly constrain the relation between the final mass of a star and the mass of its pre-stellar core; they only offer us a single time snapshot with an ensemble of cores and young stars. The masses of cores and stars can only be related statistically, by comparing the core mass function (CMF) with the stellar IMF (Salpeter 1955; Kroupa 2001; Chabrier 2005). Observations of nearby star-forming regions seem to indicate that the CMF has a similar shape as the stellar IMF, which is often interpreted as evidence in favour of the core-collapse model (e.g. Motte, Andre & Neri 1998; Alves, Lombardi & Lada 2007; Enoch et al. 2007; Nutter & Ward-Thompson 2007; Könyves et al. 2010, 2015, 2020; Marsh et al. 2016; Sokol et al. 2019; Ladjelate et al. 2020; Takemura et al. 2021, 2023). However, in more distant regions of high-mass star formation, *Herschel*’s observations (Tigé et al. 2017) and, more conclusively, interferometric surveys (e.g. Sanhueza et al. 2017, 2019; Kong 2019; Li et al. 2019; Pillai et al. 2019; Servajean et al. 2019) have revealed a scarcity of massive pre-stellar cores, implying that the mass reservoir to form high-mass stars is spread over larger scales, in contrast with the core-collapse model. To further complicate the picture, in some of the most extreme regions of high-mass star formation, the CMF at intermediate and large masses is sometimes found to be a shallower power law than the stellar IMF (Motte, Bontemps & Louvet 2018b; Pouteau et al. 2022), which would imply either core fragmentation or a shallower IMF in such regions. The observational constraints on theoretical models rely on

* E-mail: ppadoan@icc.ub.edu (PP); veli.matti.pelkonen@icc.ub.edu (VMP)

the statistical significance of the estimated values of the turnover mass and slope of the CMF. These values can be quite uncertain, as the turnover mass is often close to the completeness limit of the surveys and both turnover and slope can depend on the core-selection algorithm and may be affected by projection artefacts. The goal of this work is to assess the reliability of CMFs derived from ALMA dust-continuum observations of Galactic protoclusters. As a test bed, we use our 250 pc star formation simulation driven self-consistently by supernova (SN) explosions (Pan et al. 2016; Padoan et al. 2016a, b, 2017). The maximum resolution of the simulation is 0.0076 pc, adequate to address ALMA observations of Galactic protoclusters at a resolution of order 0.01 pc, such as those of the ALMA-IMF Large Program (Ginsburg et al. 2022; Motte et al. 2022; Pouteau et al. 2022). Although the turnover mass of the CMF is not fully resolved at this resolution (e.g. Pelkonen et al. 2021), the simulation is realistic enough to allow us to test the relation between cores selected from two-dimensional (2D) projections, as in the observations, and real cores selected from the corresponding three-dimensional (3D) volumes, irrespective of the actual value of the turnover mass.

We first analyse column-density maps obtained from the simulation, and then synthetic 1.3 mm dust-continuum maps computed with the radiative transfer code SOC (Juvela 2019). We aim at reproducing a synthetic ALMA data set and an analysis pipeline as close as possible to that of the ALMA-IMF Large Program (Ginsburg et al. 2022; Motte et al. 2022; Pouteau et al. 2022). As in Pouteau et al. (2022), the cores are extracted with the GETSF code (Men'shchikov 2021a). Cores are also extracted from the corresponding 3D volumes with a dendrogram analysis (Padoan et al. 2007; Rosolowsky et al. 2008) and compared with the sample of 2D cores from GETSF. The comparison shows that the 2D cores present a highly incomplete view of the sample of real 3D cores, are sometimes observational artefacts from projection effects, and have masses poorly correlated with those of the corresponding 3D cores.

The paper is organized as follows. In the next section we briefly summarize the simulation and in Section 3 we describe the selection and the general properties of the column density maps. The computation of the synthetic observations is presented in Section 4 and the extraction of cores in both 2D and 3D is described in Section 5. The results from the analysis of both column-density maps and synthetic observations is presented in Section 6. A discussion of our results, and their significance with respect to recent findings from the ALMA-IMF Large Program, is given in Section 7, and the main conclusions are summarized in Section 8.

2 SIMULATION

The test bed for this work is a sample of protocluster regions found in our 250 pc star formation simulation driven self-consistently by SNe. The simulation has been continuously run, during the past 3 yr, under a multiyear PRACE.¹ project, until it reached approximately 45 Myr of evolution under self-gravity. It describes an ISM region of size $L_{\text{box}} = 250$ pc and total mass $M_{\text{box}} = 1.9 \times 10^6 M_{\odot}$, where the turbulence is driven by SNe alone. Given the large time and spatial scales, the simulation develops many regions where high-mass stars are formed, including several stellar clusters.

The simulation has been shown to generate star-forming clouds with realistic observational properties, including kinematics, lifetimes, and star formation rates (Padoan et al. 2016a, b; Lu et al. 2020). It has also been used to study the statistical properties of

SN-driven turbulence (Pan et al. 2016; Padoan et al. 2016a), to propose the new *Inertial-Inflow* scenario for the formation of massive stars (Padoan et al. 2017), and to assess the real nature of massive clumps from the *Hi-GAL* Survey (Lu et al. 2022). The reader is referred to Padoan et al. (2016a, b) for details about the numerical set-up. The main features of the simulation relevant to this work are briefly summarized in the following text.

The 3D MHD equations are solved with the adaptive-mesh-refinement (AMR) code RAMSES (Teyssier 2002, 2007; Fromang, Hennebelle & Teyssier 2006), using periodic boundary conditions. The energy equation includes the pressure-volume work, the thermal energy introduced to model SN explosions, a uniform photoelectric heating as in Wolfire et al. (1995), with efficiency $\epsilon = 0.05$ and the FUV radiation field of Habing (1968) with coefficient $G_0 = 0.6$ (the UV shielding in MCs is approximated by tapering off the photoelectric heating exponentially above a number density of 200 cm^{-3}), and a tabulated optically thin cooling function constructed from the compilation by Gnedin & Hollon (2012) that includes all relevant atomic transitions. Molecular cooling is not included, due to the computational cost of solving the radiative transfer. The thermal balance between molecular cooling and cosmic-ray heating in dense gas is emulated by setting a limit of 10 K as the lowest temperature of dense gas. However, to generate synthetic observations of the dust emission, the radiative transfer is computed by post-processing individual snapshots, including all stars with mass $> 2 M_{\odot}$ as point sources (see Section 4).

The simulation is initialized with zero velocity, uniform density, $n_{\text{H},0} = 5 \text{ cm}^{-3}$, uniform temperature, $T_0 = 10^4 \text{ K}$, and uniform magnetic field, $B_0 = 4.6 \mu\text{G}$. During the first 45 Myr, self-gravity was not included and SN explosions were randomly distributed in space and time, at a rate of $6.25 \text{ SNe Myr}^{-1}$. The resolution was $\text{dx} = 0.24 \text{ pc}$, achieved with a 128^3 root grid and three AMR levels. These conditions are chosen to represent a generic Galactic spiral arm region, and the time-scale of 45 Myr is long enough to achieve a statistical steady state, prior to the inclusion of gravity. The first few SN explosions rapidly bring the mean thermal, magnetic, and kinetic energies to approximately steady-state values, with an rms magnetic field of $7.2 \mu\text{G}$, and an average of $|B|$ of $6.0 \mu\text{G}$, consistent with the value of $6.0 \pm 1.8 \mu\text{G}$ derived from the ‘Millennium Arecibo 21-cm Absorption-Line Survey’ by Heiles & Troland (2005). The minimum cell size was then decreased to $\text{dx} = 0.03 \text{ pc}$, using a root-grid of 512^3 cells and four AMR levels, for an additional period of 10.5 Myr, still without self-gravity. At $t = 55.5 \text{ Myr}$, gravity is introduced and the simulation is continued until $t \approx 100 \text{ Myr}$ with a minimum cell size further reduced to $\text{dx} = 0.0076 \text{ pc}$, by adding two more AMR levels. At this resolution, we can follow the formation of individual massive stars, so the time and location of the SNe are computed self-consistently from the evolution of those stars.

Individual stars are modelled with accreting sink particles, created when the gas density is larger than 10^6 cm^{-3} and other conditions are satisfied (see Haugbølle, Padoan & Nordlund 2018, for details of the sink particle model). An SN is created when a sink particle of mass larger than $7.5 M_{\odot}$ has an age equal to the corresponding stellar lifetime for that mass (Schaller et al. 1992). The sink particle is removed and the stellar mass, momentum, and 10^{51} erg of thermal energy are added to the grid with a Gaussian profile (see Padoan et al. 2016a, for further details). By the latest simulation snapshot used in this work, corresponding to a time of 34.7 Myr from the inclusion of self-gravity and star formation, 3942 stars with mass $> 2 M_{\odot}$ have been generated, of which 389 have already exploded as SNe. The stellar mass distribution is consistent with Salpeter’s IMF (Salpeter 1955) above $\sim 8 M_{\odot}$, but is incomplete at lower masses (it starts to

¹Partnership for Advanced Computing in Europe

flatten at a few solar masses instead of at a fraction of a solar mass), as expected for the spatial resolution of the simulation.

3 COLUMN DENSITY MAPS

The goal of this work is to study simulated star-forming regions that are comparable to observed regions of high-mass star formation. For that purpose, we select the highest column density regions from four different snapshots of the simulation, spanning a range of times between 14.2 and 34.7 Myr from the beginning of self-gravity. We generate maps of $2\text{ pc} \times 2\text{ pc}$, as that is a characteristic size of the 15 regions mapped by the ALMA-IMF Large Program. For each of the four snapshots, we find the position of maximum column density measured at a resolution of 512^2 cells, or 0.49 pc (a characteristic size of massive clumps in Csengeri et al. 2017) in the three orthogonal directions of the 250 pc computational volume. That results in 12 positions of maximum column density, which are taken as the centres of 12 maps of $2\text{ pc} \times 2\text{ pc}$. The column density maps are then recomputed at the maximum resolution of the simulation, 0.0076 pc , so each map is composed of 263×263 pixels.

We stress that these maps result from the projection of 3D columns with a very large aspect ratio of 125:1 ($250\text{ pc} \times 2\text{ pc} \times 2\text{ pc}$); while they are meant to represent relatively small star-forming regions, as those modelled with smaller simulations, they are embedded in a realistic 250 pc volume, and they contain the full projection effects to be expected at that scale. As extensively discussed in Lu et al. (2022), this projection depth is representative of the thickness and total column density of a characteristic spiral arm. Observations of similar regions in the Galactic plane and towards the Inner Galaxy may suffer much larger projection effects, as they may sample several dense regions along a distance of several kpc, rather than structures within a single spiral arm. This should be kept in mind when comparing our simulated regions with observations of the highest column density regions in the Galaxy, as discussed in the following text.

The 12 maps from the simulation are truly independent of each other, even if they are selected from only four snapshots. We have verified that only a small fraction of the 3D columns in each snapshot intersect each other. Of these, only one intersection, between directions y and z of snapshot 3, corresponds to a 3D volume whose mass gives a significant contribution to the column density in the maps. However, while the map of direction z contains most of the mass of the map in direction y , the map of direction y contains less than half of the mass of the map in direction z . Thus, even these two maps cannot be considered two different views of the same 3D region. Fig. 1 shows the 12 column density maps. The intersecting ones are shown by panels 3, y and 3, z . The map in panel 3, y shows a dominant dense filament along the z direction that seems to continue beyond the bottom of the map. The map in panel 3, z shows the projection of that filament in the z direction, and so it also includes the part of the filament that lies beyond the bottom of the map in panel 3, y .

3.1 Simulated maps as protocluster regions

All the maps in Fig. 1 appear like clusters of filaments, with the highest column densities corresponding to regions where many filaments intersect. This morphology is very similar to that of the so-called filament hubs that are ubiquitous in regions of high-mass star formation (e.g. Myers 2009; Schneider et al. 2012; Peretto et al. 2014; Kumar et al. 2020, 2022; Zhou et al. 2023). Besides the morphological similarity with the astrophysical birthplaces of massive stars, these regions are indeed forming massive stars in the simulation.

To further characterize them in relation to observed regions of high-mass star formation, we measure their mass–size relation within circular regions centred around the centre of the maps, and containing 12.5 per cent, 25 per cent, and 50 per cent of their total mass. The three circles are shown in all the maps of Fig. 1. The mass–size relation is plotted in Fig. 2 (squared symbols). These circular portions of the maps contain on average nearly 1000 M_\odot at a scale of $\sim 0.5\text{ pc}$, or a mean column density of $\sim 0.1\text{ g cm}^{-2}$. The column density tends to decrease slightly with increasing size, following approximately the slope of the empirical mass–size relation limit for high-mass star formation of Kauffmann & Pillai (2010), as revised by Dunham et al. (2011). The masses are on average a factor of 3 above the empirical limit, showing that the regions selected from the simulations have mean column densities consistent with those of observed regions forming high-mass stars.

Fig. 2 also shows the mass–size relation of the brightest ATLASGAL regions (small, black circles) from Csengeri et al. (2017), which are supposedly some of the most extreme high-mass star-forming regions in the Galaxy, and that of the 15 regions chosen for the ALMA-IMF Large Program (blue circles) of Motte et al. (2022), which are a subsample of some of the brightest regions in Csengeri et al. (2017). The median value of the column density of the ATLASGAL clumps of Csengeri et al. (2017) is a factor of 4.0 larger than that of our simulated regions, while the median column density of the even more extreme sample of the ALMA-IMF Large Program is 6.7 times larger. None the less, there is partial overlap between these Galactic protocluster regions and our simulated ones, as the lowest mean column densities from both samples are well within the largest mean values from our maps (including the case of W43-MM3, shown by the lower of the two blue filled circles in Fig. 2). The high mean *column* densities of the observed protocluster clumps may suggest very large mean *volume* densities, larger than in our simulation. However, as mentioned above and extensively discussed in Lu et al. (2022), dust emission maps of regions in the Galactic plane and towards the Inner Galaxy may suffer important projection effects with contributions from dense structures at different distances. In general, the lower depth and column density of our simulation, compared with the most extreme regions in the Inner Galactic plane, should result in less projection artefacts and spatial confusion than in those regions. Thus, our modelling approach is conservative, in the sense that the issues raised in this work may be exacerbated in real observations of Galactic protoclusters.

4 SYNTHETIC DUST-CONTINUUM MAPS

4.1 Radiative transfer

To generate the synthetic surface-brightness maps corresponding to the column-density maps of Fig. 1, we first carried out dust-continuum radiative transfer modelling of the whole 250 pc volume of each of the four snapshots with the continuum radiative transfer program SOC (Juvela 2019). Details of the radiative transfer method can be found in Lu et al. (2022), and the main points are summarized below.

The radiative transfer calculations need the density field, the dust properties, and a description of the radiation field as inputs. The density field is taken from the data cubes of the AMR simulation, and SOC uses directly the same hierarchical spatial discretization as the AMR simulation. The dust properties correspond to the Weingartner & Draine (2001) $R_V = 5.5$ dust model (Case B), where the size distribution of the carbonaceous grains extends up to $10\text{ }\mu\text{m}$. The high R_V is consistent with observations of very dense clouds, and the

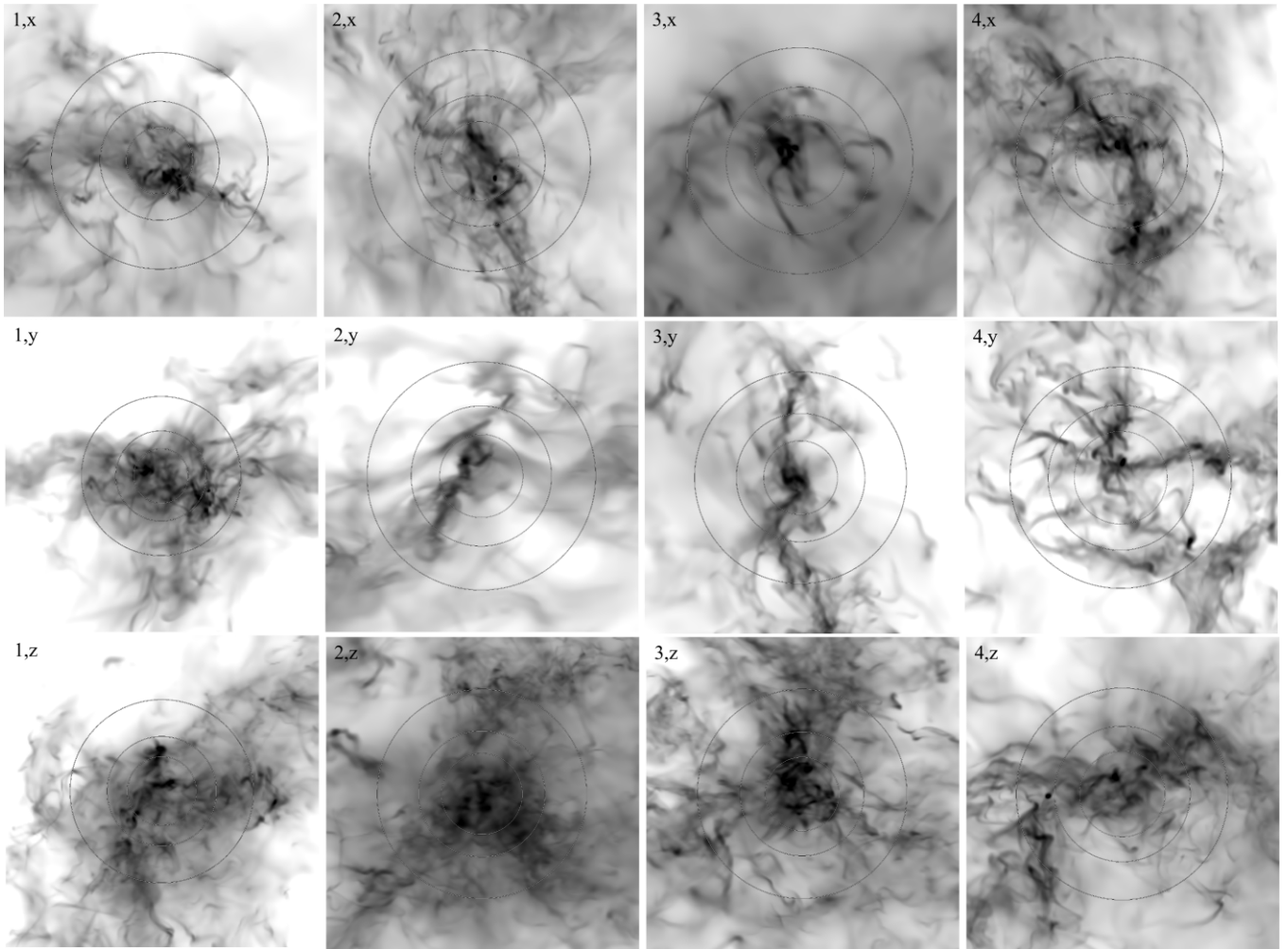


Figure 1. Column-density maps of the 12 regions analysed in this work. Each map covers a $2 \text{ pc} \times 2 \text{ pc}$ region centred around the highest column density of the corresponding projection of the whole 250 pc computational volume (see the text for details). The four columns of panels correspond to the four different snapshots of the simulation taken at time intervals of nearly 7 Myr ; the three rows of panels correspond to the three orthogonal directions. The circles show the areas containing 12.5 per cent, 25 per cent, and 50 per cent of the total mass of each map. The grey scale is proportional to the square root of the column density, with minimum and maximum values set to 0.05 g cm^{-2} (white colour) and 1.0 g cm^{-2} (black colour), respectively.

1.3 mm dust opacity of the model, $\kappa_{1.3 \text{ mm}} = 0.0037 \text{ cm}^2 \text{ g}^{-1}$, is more than twice the value of normal Milky Way dust. However, the opacity is still lower than for the Ossenkopf & Henning (1994) dust model that is discussed for comparison in Section 7.5, where $\kappa_{1.3 \text{ mm}} = 0.0083 \text{ cm}^2 \text{ g}^{-1}$. The data for the Weingartner & Draine (2001) dust models are obtained from the DustEm site² (Compiègne et al. 2011).

The radiation field consists of an isotropic external field, the Mathis, Mezger & Panagia (1983) model of the local interstellar radiation field, and of the radiation from all the stars with mass $> 2M_{\odot}$ formed self-consistently in the simulation. The number of these point sources increases with time, as star formation progresses in the simulation, and is 775, 1929, 3093, and 3942 in the four snapshots of this work. The SOC code calculates the equilibrium dust temperature of each model cell and generates the corresponding 1.3 mm surface-brightness maps for the three orthogonal view directions of each snapshot. These $250 \text{ pc} \times 250 \text{ pc}$ surface-brightness maps have a pixel size equal to 0.0076 pc , the smallest cell size of the simulation, hence they contain $32\,768 \times 32\,768$ pixels. Of these maps, only the

$2 \text{ pc} \times 2 \text{ pc}$ regions corresponding to the selected column-density maps of Fig. 1 are used for the analysis of this work.

4.2 ALMA simulations

To generate the synthetic ALMA observations, the surface-brightness maps are processed with the CASA program (v. 6.5.1), assuming a 2 kpc source distance and using an ALMA 12-m antenna configuration (*alma.cycle8.1*) that gives a beam size of 1.66 arcsec (geometric average for a source at zero declination). At equal linear resolution, this corresponds to a beam size of 0.60 arcsec at the distance of 5.5 kpc of W43, not far from the beam of 0.47 arcsec in the study of W43 by Pouteau et al. (2022). The CASA runs include simulations with the *simobserve* routine and the cleaning of the dirty interferometer image with the *tclean* routine, using automatic masking (with the *automultithresh* option), Briggs weighting with the parameter *robust* = 0, and multiscale deconvolution with the parameter *scales* = [0, 3, 9, 27]. The above steps are the same used in the study of W43 by Pouteau et al. (2022), as described in Ginsburg et al. (2022), except for the masking that was custom made. We do not

²<https://www.ias.u-psud.fr/DUSTEM/>

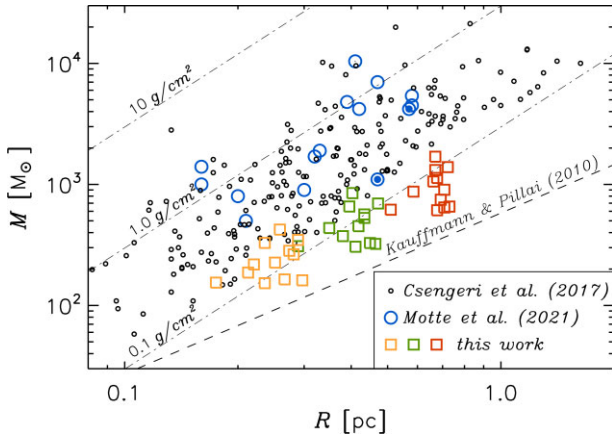


Figure 2. Mass versus size of the 12 regions analysed in this work (squared symbols). The three clusters of symbols show the values of radius and mass in the case where 12.5 per cent (yellow squares), 25 per cent (green squares), and 50 per cent (red squares) of the total mass of each map is considered (see the three circles in the panels of Fig. 1). The small, black circles correspond to the most luminous ATLASGAL regions from Csengeri et al. (2017), and the larger blue circles correspond to the masses and sizes of the 15 ALMA-IMF regions in Motte et al. (2022). The two open blue circles with a filled circle inside correspond to W43-MM2 (higher mass) and W43-MM3 (lower mass) studied in Pouteau et al. (2022). The dashed line is the empirical mass–size relation limit for massive star formation of Kauffmann & Pillai (2010), as revised by Dunham et al. (2011), and the dash–dotted lines correspond to different values of constant column density.

need to distinguish between images generated from the full 1.3 mm band and images that excludes the channels associated with lines (referred to as *bsens* and *cleanest* images, respectively, in Pouteau et al. 2022), as our surface-brightness maps do not include any contamination from emission lines. The CASA processing is carried out over an area of $3 \text{ pc} \times 3 \text{ pc}$ containing the $2 \text{ pc} \times 2 \text{ pc}$ region of interest, after doubling the number of pixels in the original surface-brightness maps, so the pixel size is approximately 0.4 arcsec, one-fourth of the beam size.

We seek to obtain a similar sensitivity as in the ALMA-IMF Large Program that was designed to reach a point-source mass sensitivity of $0.15 M_{\odot}$ at 1.3 mm (based on $T_{\text{dust}} = 20 \text{ K}$ and $\kappa_{1.3 \text{ mm}} = 0.01 \text{ cm}^2 \text{ g}^{-1}$). In the case of W43-MM2 and W43-MM3, at a distance of 5.5 kpc, the noise level is approximately $0.06 \text{ mJy beam}^{-1}$, based on table 2 in Motte et al. (2022).³ With a 6 h integration time to obtain the whole $2 \text{ pc} \times 2 \text{ pc}$ mosaic, the CASA simulations with the parameter $PWV = 0.5$ yield a noise level of $\sigma \approx 0.021 \text{ mJy beam}^{-1}$ at a distance of 5.5 kpc, three times lower than in the maps of W43 of the ALMA-IMF Large Program. However, considering that our simulated regions have a mean column density that is on average 6.7 times smaller than that of the observed regions (see Section 3.1), we further reduce the noise by averaging eight different realizations of each map, where the CASA simulations are exactly the same, except for the random thermal noise in the maps. After averaging the eight maps, the typical noise level is $\sigma \approx 0.009 \text{ mJy beam}^{-1}$, estimated by measuring the rms value of the map in small regions with negligible column density. Thus, our point-source mass sensitivity is of order $0.3 M_{\odot}$, depending on the assumed dust temperature and opacity values.

³The estimated noise level is slightly larger in table 1 of Pouteau et al. (2022), probably due to the inclusion of regions of non-negligible dust emission.

4.3 Noise reduction

Following the analysis in Pouteau et al. (2022), we further reduce the noise in the maps with the multiresolution segmentation code MNGSEG (Robitaille et al. 2019). MNGSEG separates the incoherent (Gaussian) cloud structures from the coherent component associated with the filaments and cores (see Robitaille et al. 2019). We performed the separation using a value of 2.0 for the q parameter and a skewness limit of 0.4. We then removed all the incoherent structures that were larger than the beam, as in Pouteau et al. (2022), while those at scales equal to the beam or smaller were kept. This process reduces the noise and increases the number of detected sources by more than a factor of 2. The effect of processing the images with MNGSEG is illustrated in Fig. 3, showing the synthetic ALMA images of the map 3, z of Fig. 1 before (upper panel) and after (lower panel) the noise reduction.

5 2D AND 3D CORE EXTRACTION

5.1 2D GETSF extraction

The core extraction from both the column-density maps and the synthetic ALMA maps is carried out with the GETSF code (Men’shchikov 2021a), one of the two methods used in Pouteau et al. (2022). Although several code parameters can be controlled by the user, all core (and filament) detection parameters have already been optimized and extensively tested (Men’shchikov 2021a, b), and we adopt the standard extraction parameters as in Pouteau et al. (2022), such as a maximum core ellipticity of 2 and a minimum signal to noise of 2.

For each extracted core, GETSF determines a full width at half-maximum (FWHM) ellipse and computes the total mass, $M_{c, 2D}$, in the case of column-density maps, or the total flux, $S_{1.3 \text{ mm}}^{\text{int}}$, from the surface-brightness maps. In the case of the synthetic ALMA maps, we derive the core masses from the GETSF integrated flux assuming the 1.3 mm emission is optically thin:

$$M_{c, 2D} = \frac{S_{1.3 \text{ mm}}^{\text{int}} d^2}{\kappa_{1.3 \text{ mm}} B_{1.3 \text{ mm}}(T_{\text{dust}})}, \quad (1)$$

where d is the distance to the source, $\kappa_{1.3 \text{ mm}}$ is the dust opacity, $B_{1.3 \text{ mm}}$ is Planck’s law, and T_{dust} is the dust temperature (Hildebrand et al. 1977). Although Pouteau et al. (2022) include a correction for optically thick emission (Motte et al. 2018a), they find that the correction is significant for only two of their cores (with a change in the estimated mass of only 15 per cent), and we have verified that in our core samples that correction is always negligible. The dust opacity values are $\kappa_{1.3 \text{ mm}} = 0.0037 \text{ cm}^2 \text{ g}^{-1}$ for the dust model of Weingartner & Draine (2001) and $\kappa_{1.3 \text{ mm}} = 0.0083 \text{ cm}^2 \text{ g}^{-1}$ for the dust model of Ossenkopf & Henning (1994). For the temperature, we use a single value for all cores, $T_{\text{dust}} = 13.0 \text{ K}$ for the dust model of Weingartner & Draine (2001) and $T_{\text{dust}} = 7.5 \text{ K}$ for the dust model of Ossenkopf & Henning (1994), corresponding to the median dust temperature of the candidate 3D cores, defined in Section 6.1.1 as the main overdensity in the line of sight of each GETSF core. All the analysis and figures in this work are based on the synthetic ALMA images from the dust model of Weingartner & Draine (2001). A comparison between the two dust models is shown in Section 7.5.

We do not use the individual temperatures of the candidate 3D cores because they are not observable quantities. The colour temperature can be derived from observations at different wavelengths, but we find that it does not accurately reflect the real dust temperature variations from core to core (see Section 7.5), so there is no advantage in using it. Although in Pouteau et al. (2022) the core masses are

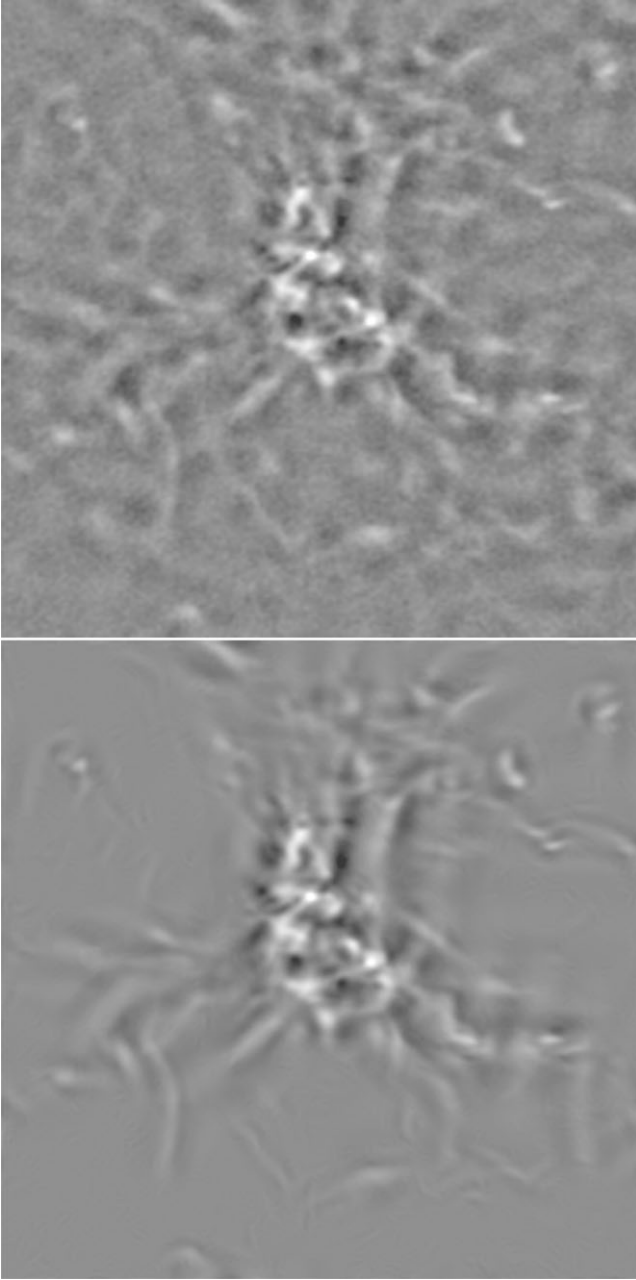


Figure 3. Example of the effect of noise reduction by the MNGSEG code on the map corresponding to the panel 3, z of Fig. 1. The upper panel is the simulated ALMA image before the noise reduction, the lower panel the image processed with MNGSEG. The grey scale is proportional to the surface brightness, with minimum and maximum values set to 5.0 MJy sr^{-1} (black colour) and $100.0 \text{ MJy sr}^{-1}$ (white colour), respectively.

based on estimates of individual core temperatures, we adopt a single value of T_{dust} also to estimate the core masses from the observations of the W43 region in Section 7.3. Using a single value of T_{dust} , the derived masses are proportional to the integrated fluxes with the same constant of proportionality for all cores (see equation 1). Thus, we effectively compare the integrated flux distributions rather than the CMFs, avoiding the extra uncertainty arising from the temperature determination.

FWHM ellipses of the cores extracted by GETSF from one of our column-density maps and the corresponding synthetic ALMA map

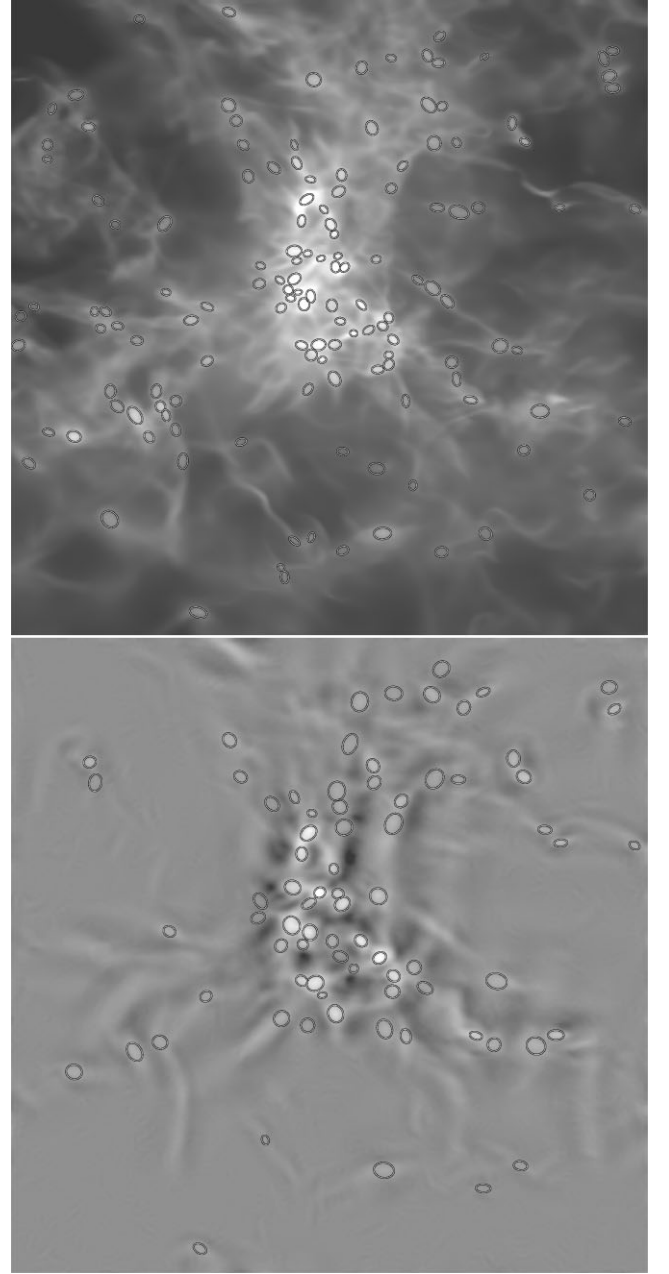


Figure 4. Examples of GETSF core selection on a column density map (upper panel) and the corresponding synthetic ALMA map after noise reduction (lower panel), corresponding to the panel 3, z of Fig. 1. The grey scale is proportional to the square root of the column density (upper panel) or surface brightness (lower panel), with minimum and maximum values set to 0.05 g cm^{-2} (black colour) and 1.0 g cm^{-2} (white colour) in the upper panel and 5.0 MJy sr^{-1} (black colour) and $100.0 \text{ MJy sr}^{-1}$ (white colour) in the lower panel. The ellipses correspond to the FWHM of the cores extracted by GETSF.

are shown in the two panels of Fig. 4, which correspond to the panel 3, z of Fig. 1. The cores appear to follow the densest filaments and concentrate in the densest areas where multiple filaments intersect, as usually found in real Herschel and ALMA observations. Some of the same cores can be recognized in both images, but there are also several cases of sources extracted from the column-density map that are not seen in the synthetic ALMA map and vice versa.

5.2 3D DENDRO extraction

To extract the 3D cores from the $2\text{ pc} \times 2\text{ pc} \times 250\text{ pc}$ columns of each map, we use the clumpfind algorithm introduced in Padoan et al. (2007). To avoid confusion with other clumpfind algorithm in the literature, we here refer to this algorithm as DENDRO for the first time. While the algorithm was designed to select gravitationally unstable cores (see Pelkonen et al. 2021), it can also be used as a straightforward dendrogram (Rosolowsky et al. 2008), without imposing a gravitational instability condition while building the tree. In this case, cores are simply defined as connected overdensities that cannot be split into two or more overdensities of amplitude $\delta n/n > f$. DENDRO scans the density field with discrete density levels, each of amplitude f relative to the previous one. Only the connected regions above each density level are retained. The final (unsplit) core of each branch is retained. Each core is assigned only the mass within the density isosurface that defines the core (below that density level the core would be merged with its next neighbour).

The DENDRO algorithm depends only on three parameters: (1) the spacing of the discrete density levels, f , (2) the minimum density above which cores are selected, n_{\min} , and (3) the minimum number of cells per core. In principle, there is no need to define a minimum density, but in practice it speeds up the algorithm. In this work, we adopt $n_{\min} = 10^4\text{ cm}^{-3}$, which is appropriate for pre-stellar cores. The parameter f is set by looking for numerical convergence of the mass distribution with decreasing values of f . We find that the mass distribution above approximately 1 M_{\odot} is stable in the range of values between $f = 32$ per cent and $f = 2$ per cent⁴, while at the lowest masses the number of cores slightly increases with decreasing f , but with a clear tendency to converge at around $f = 2$ per cent. However, these variations in the CMFs do not cause significant variations in our comparison between 2D and 3D cores, so the qualitative conclusions of this work do not depend on the precise value of f . The plots in this work correspond to the DENDRO runs with $f = 8$ per cent. The minimum number of cells is set to 27, to ensure that all the detected cores are at least minimally resolved in the simulation and to limit the minimum mass and size of 3D cores to values comparable to those of the 2D cores extracted by GETSF.

Because GETSF distinguishes between sources and filaments, sources cannot have an aspect ratio larger than two. DENDRO does not impose a limit on the aspect ratio of the cores. However, we have verified that core elongation is not a problem in comparing with the GETSF 2D cores. For each 3D core, we have measured the half-mass distance of all its cells from its centre and the equivalent radius. For elongated cores and filaments, the half-mass distance can be much larger than the equivalent radius. However, we find that an insignificant number of the 3D DENDRO cores have a ratio of half-mass distance over equivalent radius larger than two.

6 RESULTS

We present separately the results of the source extraction from the column-density maps and from the synthetic ALMA maps. The idealized case of the column-density maps provides a test of projection effects in isolation, without the observational complications, such as radiative transfer effects, interferometric artefacts, and instrumental noise. These observational effects are then addressed in the second

part of this section where the analysis of the synthetic ALMA maps is presented.

6.1 Cores from column density maps

6.1.1 GETSF runs and candidate 3D cores

Using GETSF we extract 1534 compact sources from the 12 column density maps, convolved with a beam size corresponding to 0.60 arcsec at the distance of 5.5 kpc of W43. We want to test if these cores correspond to real 3D cores, and, if so, how their masses compare with the corresponding 3D ones. One could directly search for overlap between 3D cores and 2D ones by simply projecting the positions of the 3D cores on the 2D maps. However, we find it more instructive to go through the extra step of first identifying a candidate 3D core position along the line of sight of each 2D core. This extra step provides a test of the quality of the background subtraction by GETSF, even when a counterpart real 3D core is not found. The GETSF background subtraction turns out to be rather impressive, in the sense that real 3D density structures are discovered by GETSF even if the background is often ~ 90 per cent of the mass in the line of sight.

To identify a candidate 3D core position, we first search for the density maxima along the line of sight of each GETSF core, scanning its full 250 pc length. The density is first averaged within the footprint of the core in the two directions on the plane of the sky, to obtain a 1D array of $32\,768$ elements, and a physical length of 250 pc . Each element of this array corresponds to the mean density on a slice of thickness equal to 0.0076 pc (the minimum cell size in the simulation) and area equal to the area of the core's footprint. The position of the highest density in this 1D array is chosen as the candidate 3D core position. We also define a candidate 3D core, as the spherical region centred around that position in the line of sight, and with radius equal to the footprint radius of the corresponding GETSF core. We refer to the mass of this 3D candidate core as $M_{\text{cand}, 3\text{D}}$. We repeat the process also for the second and third highest density maxima along the line of sight, so these other density peaks can also be considered when searching for an associated 3D core (see Section 6.1.2).

The comparison of the 2D GETSF masses with those of the corresponding candidate 3D cores is shown in the upper panel of Fig. 5. The dashed line shows the one-to-one relation, while the thick solid line is a least-squares fit corresponding to the relation $M_{\text{c}, 2\text{D}} = 0.91 M_{\text{cand}, 3\text{D}}^{0.97}$ (where the mass unit is 1 M_{\odot}). For any given value of $M_{\text{cand}, 3\text{D}}$, the error in the estimated mass, $M_{2\text{D}}$, is quite small. The standard deviation of $M_{2\text{D}}$ relative to the best fit in the logarithmic plot corresponds to a mass ratio of less than a factor of 1.3, the correlation is almost exactly linear, and the normalization at 1 M_{\odot} almost unity. Considering that the background subtraction performed by GETSF is on average quite large (approximately 90 per cent of the mass in the line of sight is interpreted as background in most cases), GETSF is very successful at extracting the mass of the dominant 3D dense structure along the line of sight. This also implies that the estimated volume density based on the GETSF mass and GETSF core size is also quite accurate, despite the complexity of the cloud morphology.

The success of GETSF to identify real high-density structures along the line of sight does not necessarily mean that most GETSF cores correspond to actual 3D cores of a similar mass, nor that most of the real 3D cores are captured in 2D by GETSF. There is no guarantee that the boundary of a candidate 3D core (a spherical volume of size equal to that of the GETSF core) corresponds to that of a core selected independently by a different 3D extraction algorithm. For example, a candidate 3D core may be a segment of a filament that happens to

⁴In the range of masses between 1 and 10 M_{\odot} , the slopes of the mass distributions computed with $f = 2$ per cent and $f = 8$ per cent differ by only 4 per cent.

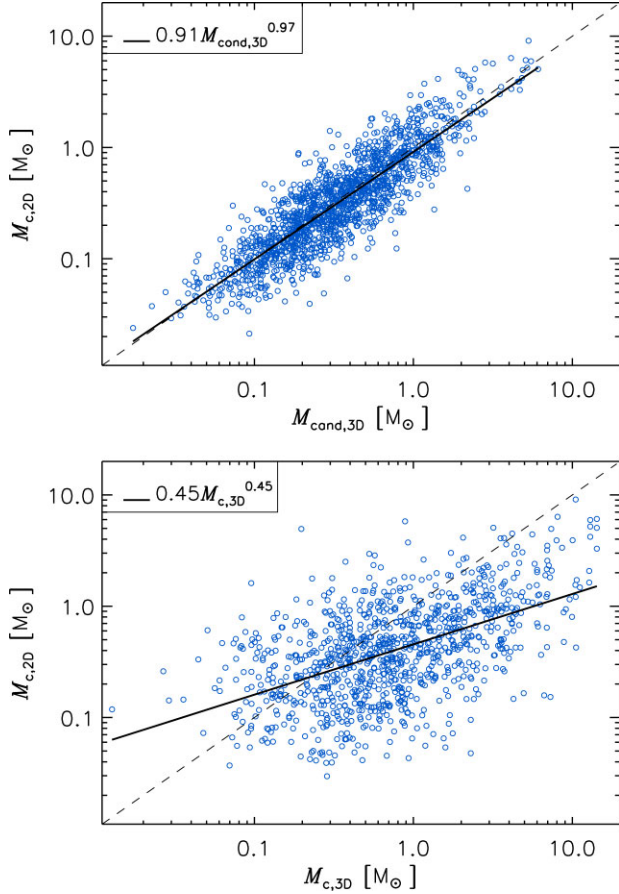


Figure 5. Comparison of the mass of cores selected by GETSF from the column-density maps, $M_{c,2D}$, and the mass of the corresponding candidate 3D cores along the line of sight, $M_{cand,3D}$ (upper panel), or the mass of the overlapping DENDRO cores extracted independently in the 3D data cube, $M_{c,3D}$ (lower panel). The dashed lines correspond to equal masses, and the thick solid lines to the least-squares fits. In the upper panel, all 1534 GETSF cores are shown, while the lower panel is limited to the 1023 overlapping GETSF and DENDRO cores.

intersect another filament in projection (not in 3D), hence appearing as a bona fide 2D core. That filament segment with size equal to that of the GETSF core may indeed have a similar mass as that of the GETSF core, but it is not a real 3D core. Even when a candidate 3D core overlaps with a real 3D core, its mass (or that of the associated GETSF core) may not be a reliable estimate of that of the real 3D core, as the latter could have a significantly different size or centre of mass. In addition, a majority of real 3D cores will generally be missed in 2D projections if they frequently overlap along the line of sight. Thus, to truly test the quality of the 2D source extraction relative to real 3D cores, we need to also independently extract 3D cores from the 3D data cubes that were used to generate the column-density maps. For that purpose, we use the DENDRO algorithm as described in Section 5.2.

6.1.2 DENDRO runs and real 3D Cores

DENDRO returns a total of 7298 3D cores (for $f = 8$ per cent) from the 12 maps, a much larger number than found in 2D, as to be expected. The range of sizes and masses of the 3D cores are quite similar to those of the GETSF cores. The median mass is $0.25 M_{\odot}$, versus $0.27 M_{\odot}$ for the GETSF cores. We search for spatial overlap between the GETSF cores and the DENDRO cores using the coordinates

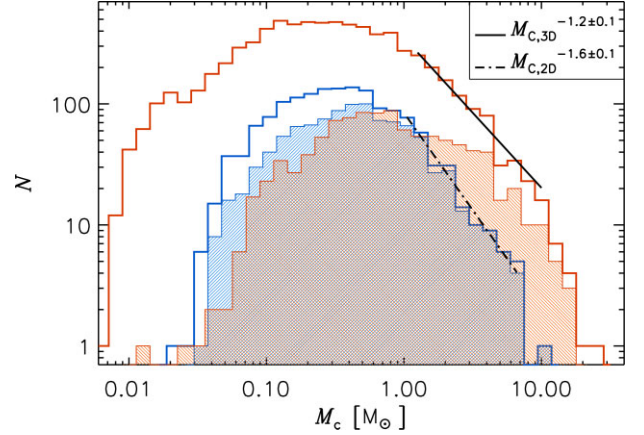


Figure 6. Mass distributions of the 3D DENDRO cores (red histograms), and of the 2D GETSF cores selected from the column-density maps (blue histograms). The unshaded histograms are for the full core samples, while the shaded ones are for the sub-samples of DENDRO cores (red histogram) and GETSF cores (blue histogram) that overlap with each other. Power-law fits in the approximate mass interval $1\text{--}10 M_{\odot}$ are shown for the CMFs of the full samples.

of the candidate 3D cores, as those cores are interpreted as the best 3D counterpart of the GETSF cores. If the centre of a DENDRO core is found inside the volume of a candidate 3D core, then that DENDRO core is taken as the 3D counterpart to the corresponding GETSF core. If that condition is not satisfied, the test is repeated using the candidate cores associated with the second highest density peak in the line of sight, and failing also that the third highest density peak is tested (see Section 6.1.1). We do not consider even lower density peaks below the third highest ones, because then the association with the DENDRO core is deemed to be insignificant (and indeed the correlation between the two 2D and 3D core masses would be negligible). Based on this criterion, we find a total of 1023 overlapping cores, which is 67 per cent of the GETSF cores and 14 per cent of the DENDRO cores.

The comparison of the masses of this subset of cores is shown in the lower panel of Fig. 5. The least-squares fitting gives the relation $M_{c,2D} = 0.45 M_{c,3D}^{0.45}$ (with a mass unit of $1 M_{\odot}$). The vertical scatter in this plot is much larger than that in the upper panel, with a standard deviation relative to the best fit corresponding to a factor of 4 in mass. The fit is now significantly shallower than linear, and Pearson's correlation coefficient has decreased from 0.87 in the upper panel to 0.53 in the lower one. For each value of the 3D core mass, $M_{c,3D}$, the corresponding mass of the overlapping GETSF core, $M_{c,2D}$, spans a total range of nearly two orders of magnitude, not much smaller than the full range of GETSF core masses. Thus, the GETSF masses are rather unreliable estimates of the masses of the corresponding DENDRO cores, even if there is still a significant statistical correlation between the two masses.

6.1.3 Core mass functions

Given that the number of DENDRO cores is so much larger than that of the GETSF cores, the great majority of the 3D cores (86 per cent) are not found in 2D, so the GETSF sample is highly incomplete. Fig. 6 shows the CMFs of the 3D DENDRO cores (thick red line) and of the 2D GETSF cores (thick blue line). The number of 2D cores is always much smaller than the number of 3D cores, at any mass. The shape of the two CMFs are also somewhat different. In the range between approximately 1 and $10 M_{\odot}$, the 2D CMF is significantly steeper,

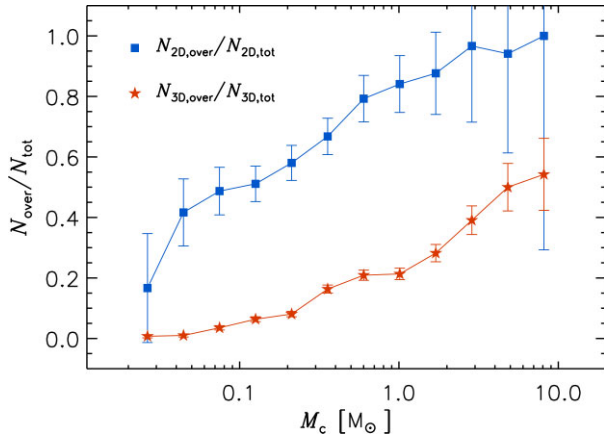


Figure 7. Fraction of cores with overlap between the DENDRO selection and the GETSF selection in the column-density maps, as a function of core mass. The blue squares are the fraction with respect to the total number of GETSF cores in each mass interval, $N_{2D, \text{over}}/N_{2D, \text{tot}}$, and the red stars the fraction with respect to the total number of DENDRO cores, $N_{3D, \text{over}}/N_{3D, \text{tot}}$. The error bars are the propagation of the Poisson errors of the individual quantities.

with a slope of -1.6 ± 0.1 , than the 3D CMF that has a slope of -1.2 ± 0.1 . The peak of the 3D CMF would certainly shift to lower masses if the numerical resolution of the simulation were increased (e.g. Pelkonen et al. 2021), as more 3D cores of low mass would be found. However, assuming a fixed telescope beam size, the peak of the 2D CMF may not shift much towards lower masses even if the numerical resolution were increased, because the assumed telescope beam size in the GETSF search is already twice larger than the current resolution of the simulation.

The CMFs of the 1023 2D and 3D cores that are found to overlap with each other are shown by the shaded histograms in Fig. 6. The 3D CMF (red histogram) is clearly shifted to larger masses than the 2D CMF (blue histogram). The ratio of the 3D CMF of overlapping cores with the 3D CMF of all cores is shown by the red star symbols in Fig. 7. The plot shows that below approximately $0.5 M_\odot$ less than 20 percent of the 3D cores are found by GETSF in 2D, as clearly illustrated by the comparison of the shaded and unshaded red histograms in Fig. 6. The ratio increases monotonically with core mass, up to nearly 0.6 at the largest masses.

Finally, the ratio of overlapping 2D cores and all 2D cores, shown by the blue squares in Fig. 7, gives the fraction of 2D cores that can be considered as real, rather than projection effects. This ratio is close to 1 above approximately $2 M_\odot$, but decreases monotonically with decreasing core mass. At $0.1 M_\odot$, approximately half of the cores are projection artefacts.

6.2 Cores from synthetic 1.3 mm ALMA maps

6.2.1 ALMA GETSF runs and candidate 3D cores

We now consider the GETSF core extraction from the synthetic 1.3 mm ALMA maps corresponding to the column-density maps studied above. We refer to these 2D cores also as synthetic ALMA cores. The GETSF search yields a total of 791 synthetic ALMA cores, an average of 66 cores per map. The maps with the smallest and largest numbers of cores have 40 and 80 cores, respectively. The reduced number of synthetic ALMA cores with respect to the number of cores from the column-density maps is to be expected, because the observational noise sets a finite mass sensitivity.

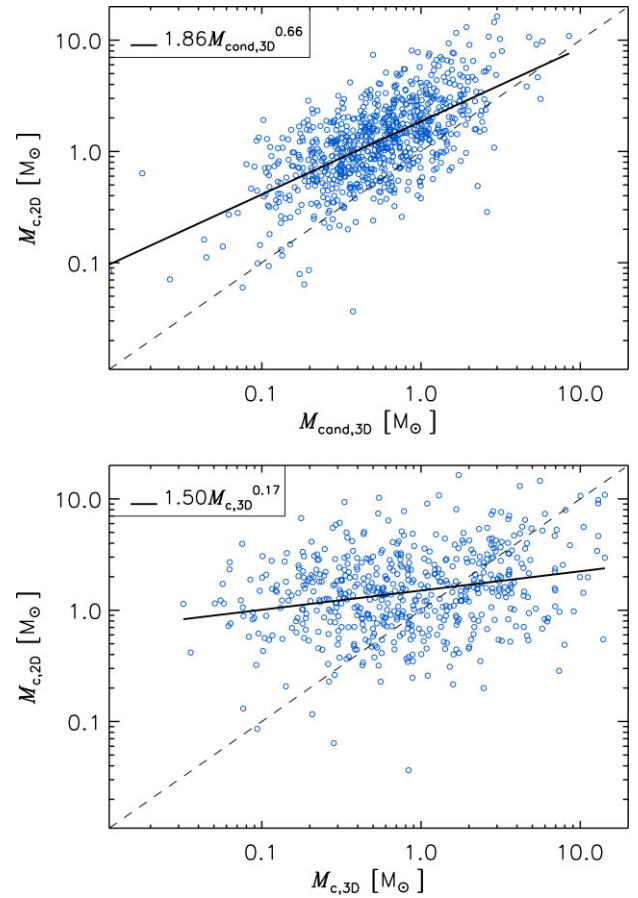


Figure 8. Comparison of the mass of cores selected by GETSF from the synthetic ALMA maps, $M_{c,2D}$, and the mass of the corresponding main 3D cores along the line of sight, $M_{\text{main},3D}$ (upper panel), or the mass of the overlapping cores selected independently in the 3D data cube, $M_{c,3D}$ (lower panel). The dashed lines correspond to equal masses, and the thick solid lines correspond to the least-squares fits. In the upper panel, all 791 GETSF cores are shown, while the lower panel is limited to the 557 GETSF cores that overlap with a corresponding 3D DENDRO core.

Using the positions and sizes of the synthetic ALMA cores, we repeat the same study of density fluctuations in the line of sight of the GETSF cores as in the case of the column-density maps (see Section 6.1.1). The upper panel of Fig. 8 compares the 2D GETSF masses with those of the corresponding candidate 3D cores, where the dashed line shows the one-to-one relation and the thick solid line is a least-squares fit. Although the vertical scatter is increased with respect to Fig. 5, there is still a significant correlation between the two masses, with a Pearson’s correlation coefficient of 0.64. However, the least-squares fit gives the relation $M_{c,2D} = 1.86 M_{\text{cand},3D}^{0.66}$ (where the mass unit is $1 M_\odot$), much shallower than linear, and the GETSF masses are on average 2.3 times larger than those of the candidate 3D cores (based on the ratio of the median values), suggesting a smaller background subtraction than in the case of the column-density maps, possibly caused by interferometric artefacts, as discussed in Section 7.2.

6.2.2 ALMA DENDRO runs and real 3D cores

Following the same procedure as in Section 6.1.2 for the case of the column-density maps, we identify the 3D DENDRO cores that are associated with the synthetic ALMA cores extracted with GETSF. As in Section 6.1.2, the criterion is that the centre of the DENDRO

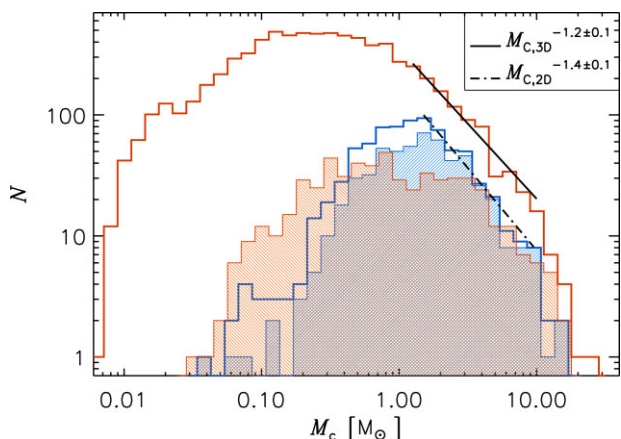


Figure 9. Mass distributions of the 3D-selected cores (red histogram), and of the GETSF cores selected from the synthetic ALMA maps (blue histogram). The unshaded histograms are for the full core samples, while the shaded ones are for the subsamples of 557 3D cores (red) and GETSF ALMA cores (blue) that overlap with each other. Power-law fits in the approximate mass interval $1.5\text{--}10\text{ M}_\odot$ are shown for the CMFs of the full samples.

core must be inside the spherical volume of the candidate 3D core associated with the GETSF core. This search yields 557 overlapping cores, corresponding to 70 per cent of the synthetic ALMA cores, or 8 per cent of the 7298 DENDRO cores. The lower panel of Fig. 8 shows the comparison of the masses of the synthetic ALMA cores, $M_{c,2D}$, with those of the corresponding 3D cores, $M_{c,3D}$. The scatter in this plot is very large, and the two masses are barely correlated, with a Pearson’s coefficient of 0.25, and an almost flat slope of the least-squares fit, $M_{c,2D} = 1.50 M_{c,3D}^{0.17}$ (where the mass unit is 1 M_\odot). Despite the fact that 70 per cent of the synthetic ALMA cores have a real 3D counterpart (and approximately 90 per cent above 2 M_\odot), their mass does not really reflect that of the corresponding 3D cores.

We have verified that the correlation of the two masses remains rather low (Pearson’s coefficient of 0.35) even if the GETSF masses were derived from the 1.3 mm fluxes using the actual dust temperature of the candidate 3D cores (an ideal knowledge that could not be achieved from the observational data). Thus, the temperature uncertainty is only a partial contribution to the scatter, which is dominated by projection effects and by the differences between the 2D and 3D core definitions (as in the lower panel of Fig. 5) and by interferometric artefacts (see Section 7.2). However, temperature variations along the line of sight certainly make projection effects and background subtraction more complex than in the case of the column density maps.

6.2.3 ALMA CMFs

The mass distribution of the synthetic ALMA cores is shown by the unshaded blue histogram in Fig. 9. The CMFs of the 3D DENDRO cores is shown by the red unshaded histogram, while the shaded histograms show the CMFs of the subsamples of the 557 ALMA cores (blue) and 3D cores (red) that overlap with each other. In the range of masses where the CMF of the synthetic ALMA cores is close to a power law, approximately between 1.5 and 10 M_\odot , its slope is -1.4 ± 0.1 , significantly shallower than that of the GETSF cores from the column-density maps and only slightly steeper than that of the 3D DENDRO cores. Above approximately 1 M_\odot , the number of synthetic ALMA cores is significantly larger than that of the 2D cores from the column-density maps (see Fig. 6), and only less than

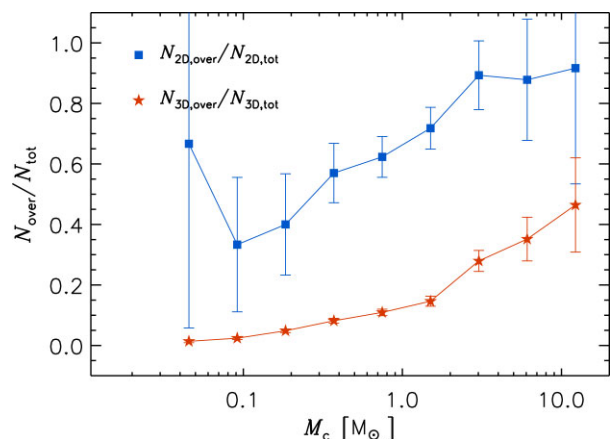


Figure 10. Fraction of cores with overlap between the 3D selection and the GETSF selection in the synthetic ALMA maps, as a function of core mass. The blue squares are the fraction with respect to the total number of GETSF cores in each mass interval, $N_{2D,over}/N_{2D,tot}$, and the red stars the fraction with respect to the total number of 3D cores, $N_{3D,over}/N_{3D,tot}$. The error bars are the propagation of the Poisson errors of the individual quantities.

a factor of 3 lower than the number of 3D cores of the same mass. The reason for this excess of massive ALMA cores relative to those from the column-density maps may be related to non-trivial effects of interferometric artefacts, as discussed below in Section 7.2.

The plot with blue-square symbols in Fig. 10 shows the ratio of the numbers of synthetic ALMA cores with a real 3D counterpart and the total number of synthetic ALMA cores, within each mass interval. Overall, 70 per cent of the synthetic ALMA cores have a 3D counterpart. Above 2 M_\odot , 88 per cent have a 3D counterpart or, conversely, only 12 per cent may be interpreted as projection artefacts. Towards lower masses, the fraction decreases monotonically (except for the smallest mass bin that is not statistically significant), down to a value of approximately 35 per cent at approximately 0.1 M_\odot .

The ratio between the 3D CMF of overlapping cores and the 3D CMF of all cores (shaded and unshaded red histograms in Fig. 9) is shown by the red-star symbols in Fig. 10. This ratio corresponds to the completeness fraction of the observational CMF. The fraction decreases monotonically with decreasing mass, as in Fig. 7, from 40 per cent at the largest masses, to 15 per cent at 1 M_\odot , to 5 per cent or less below approximately 0.1 M_\odot , near the empirical sensitivity limit of the synthetic ALMA maps. Evidently, the synthetic ALMA observations yield a highly incomplete sample of the real 3D cores. As to be intuitively expected, the completeness fraction decreases with decreasing mass at all masses. However, this does not result in a shallower 2D CMF relative to the 3D CMF at large masses, as trivially expected, because of the lack of correlation between 2D and 3D masses (Fig. 8). In other words, when comparing the blue and red unshaded histograms in Fig. 9, the GETSF cores corresponding to the 3D DENDRO cores are not in the same mass bins in the two CMFs. This also means that the similar slopes of the two CMFs above approximately 1.5 M_\odot is essentially a coincidence: projection effects, 2D versus 3D core definitions, interferometric artefacts, and radiative transfer effects (see Section 7) transform the steep CMF of the 2D cores of the column density maps into a much shallower CMF of synthetic ALMA cores. Nevertheless, if the similarity in the slopes were confirmed as a general result, in practice one could use the observed slope as a rough estimate of the true slope of the CMF of 3D cores.

The continuous variation with mass of the completeness fraction of our synthetic core sample runs contrary to estimates for observational

surveys of compact sources, where completeness fractions are usually of order unity above a minimum mass (e.g. André et al. 2010; Motte et al. 2018b; Pouteau et al. 2022), while it is consistent with what is found in the case of more extended cores (e.g. Cao et al. 2021). But we stress again that a simple correction of the CMF slope based on the mass-dependence of the completeness fraction is inadequate due to the lack of statistical correlation between 2D and 3D masses.

7 DISCUSSION

7.1 Individual effects

We aim at evaluating the relative impact of different effects on the correlation between the GETSF ALMA core masses and the DENDRO 3D core masses shown in the bottom panel of Fig. 8. For that purpose, besides the column-density maps and the synthetic ALMA maps discussed in Sections 6.1 and 6.2, we also generate and analyse three more full sets of maps: single-dish, synthetic surface-brightness maps without thermal noise at 1.3 mm with the same dust model (Weingartner & Draine 2001) and the same beam size (0.60 arcsec at 5.5 kpc) as the ALMA synthetic observations, synthetic ALMA images without thermal noise, and synthetic ALMA images with thermal noise, but without the noise reduction from the MNGSEG code. Synthetic cores are extracted with GETSF from each of these new sets of 12 maps, and the core masses are derived from equation (1) with the same $\kappa_{1.3\text{ mm}}$ and T_{dust} values as for the synthetic ALMA cores (see Section 5.1).

Including the DENDRO extractions from the 3D density cubes, we thus have six samples of cores, whose masses we refer to as M_i , with $i = 1$ to 6, in the following text. By comparing different core samples with each other, we can separate the contribution of different effects to the CMF. We consider these effects as consecutive steps in order of increasing complexity: projection effect (from the 3D cubes to the column density maps), temperature effect (from the column density to the single-dish surface brightness maps), (u,v) sampling effect (from the single-dish to the interferometric maps, without noise), noise effect (from the interferometric maps without thermal noise to the same maps with noise), and noise-reduction effect (from the interferometric maps without thermal noise to the same maps with noise first added, and then reduced with the MNGSEG code). We focus on the correlation of core masses between two consecutive steps in the order given above. These steps are summarized in Fig. 11, where Pearson's correlation coefficient of each step is also given.

Strictly speaking, the correlation between the initial masses M_1 (the 3D DENDRO cores) and the final masses M_6 (the GETSF ALMA cores) cannot be derived as the product of the individual steps. For example, the completeness fraction is not exactly the product of the individual completeness fractions, because cores that do not have a counterpart in the previous step may have a counterpart in the step before the previous one. However, we find that the product of the four correlation coefficients (excluding the case of noise without noise reduction that is shown here only as an alternative to the last step) is nearly identical to the correlation coefficient between M_1 and M_6 : $r_{1,2}r_{2,3}r_{3,4}r_{4,6} = 0.255$, while $r_{1,6} = 0.251$, and the product of the individual completeness fractions is also a good approximation to the completeness fraction in Fig. 10. Therefore, we are confident that this approach provides a good estimate of both the absolute and relative importance of each effect. The scatter plots between the pairs of masses M_i and M_j are shown in the five panels of Fig. 12, where the thick black lines are the least-squares fits with values shown in the legend. The green circles show the M_i masses of cores

M_i	Extraction	Effect	r
M_1	3D cube		
		projection	0.53
M_2	column density		
		temperature	0.79
M_3	single dish		
		u,v sampling	0.85
M_4	interferometer		
		thermal noise	0.62
M_5	ALMA		
		denoising	0.72
M_6	ALMA denoised		

Figure 11. Schematic illustration of the different definitions of core masses, M_i , adopted in Fig. 12. The second column specifies the type of maps where the cores with masses M_i are extracted from, the third column gives the main effect addressed by the comparison of core masses extracted in two consecutive ways, and the fourth column gives Pearson's correlation coefficient between the corresponding masses. 'Single dish' stands for the beam-convolved surface brightness maps without noise, 'interferometer' the simulated ALMA maps without noise, 'ALMA' the simulated ALMA maps including thermal noise, and 'ALMA denoised' the ALMA simulated maps with noise, where the noise has been reduced with the MNGSEG code.

with an M_j counterpart (overlapping cores). The fraction of i cores with a j counterpart (completeness fraction), as a function of mass, is shown by the red stars, and the fraction of j cores with an i counterpart (interpreted as the fraction of real cores) is shown by the blue squares, as in Figs 7 and 10 (their values are given by the y-axis on the right-hand side of the panels). Each panel also shows the CMFs for the M_i masses (light grey histograms), and for the M_j masses (thick black histograms).⁵

The comparison of the five panels shows that the projection effect (top panel) has the strongest impact, meaning the lowest correlation coefficient as well as the lowest completeness fraction at large masses. It also generates a significant number of artefacts at low masses, as well as a steepening of the CMF, as already discussed in Section 6.1.2. Based on correlation coefficient, slope, and completeness, the second strongest effect is noise. Comparing the two bottom panels, one can see that the noise reduction increases the correlation as well as the completeness at all masses, but at the price of a significant increase in the number of artefacts. While the case without noise reduction has essentially no artefacts, in the case with noise reduction the number of artefacts increases monotonically with decreasing mass, reaching approximately 30 per cent already at 1 M_{\odot} .

The effects of temperature and (u,v) sampling are comparable, both contributing to the CMF slope getting a bit shallower than that of the cores from the column-density maps. The (u,v) sampling effect is the main cause for the net shift of the CMF towards larger masses by approximately a factor of 2, which is further discussed in Section 7.2. The contributions to the completeness and artefact fractions from the two effects are similar, with all four plots approximately monotonic across all mass values.

⁵For the grey histograms the x-axis label is correct, while the y-axis label should be $N(M_i)$, and for the black histograms (as well as the blue-squares plots) the y-axis labels are correct, while the x-axis label should be M_j .

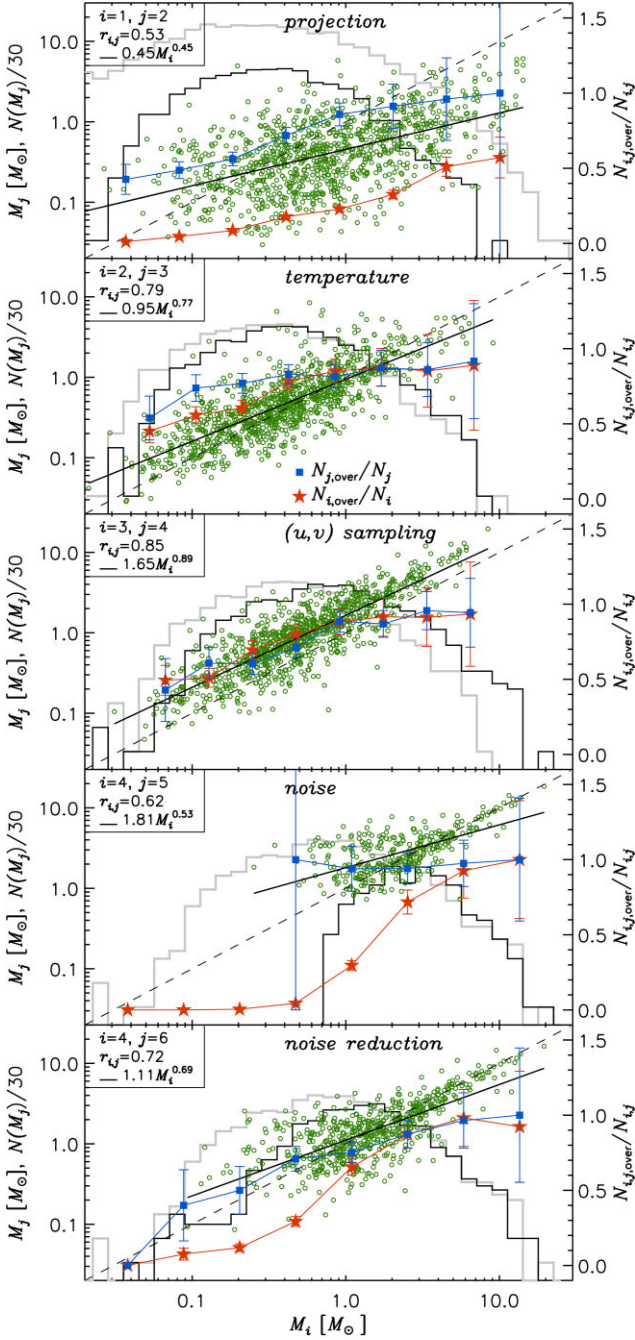


Figure 12. Scatter plots for masses of cores extracted in different ways, to highlight the different effects that contribute to the relation between the 3D DENDRO cores and the GETSF ALMA cores shown in Fig. 8. The definitions of the different masses, M_i , are given in Fig. 11 and further explained in the main text. The thick solid lines are the least-squares fits, whose results are reported in the legend, together with Pearson’s correlation coefficients, $r_{i,j}$, for each pair of masses, M_i and M_j . The light grey histograms show the mass distributions for the masses M_i , while the thick black histograms show those of the masses M_j . The blue squares are the fraction of j cores that have an i counterpart (so they are not artefacts with respect to the i cores), and the red stars the fraction of i cores with a j counterpart (the completeness fraction), as in Figs 7 and 10, with values given by the y -axis on the right-hand side of the plots (notice that the x -axis is labelled as M_i , but in the case of the black histograms and the blue squares it should be M_j).

7.2 Interferometric artefacts

We have shown in Section 6.2.3 that the CMF of the synthetic ALMA cores has an excess of high-mass cores and a slightly shallower power-law tail relative to the CMF extracted from the column-density maps (blue unshaded histogram in Fig. 9 versus blue unshaded histogram in Fig. 6). The shift in the turnover mass depends on the noise level that sets a mass sensitivity: the higher the noise, the higher the turnover mass. But the high-mass tail of the CMF is also shifted to the right (larger masses). Two straightforward explanations for this excess of massive cores are possible: (i) the observational noise causes an artificial merging of nearby cores extracted by GETSF; (ii) the shift is due to an incorrect choice of the temperature (assumed to be too low). However, the comparison of the different CMFs in the panels of Fig. 12 proves that neither of these simple explanations is correct.

The comparison of the two pairs of CMFs in the two bottom panels of Fig. 12 shows that the effect of thermal noise is the expected one: the sensitivity of the images is reduced and so the CMF turnover shifts to larger masses, meaning that lower mass cores are lost from the sample. But that loss does not cause an artificial merging into larger mass cores, as the high-mass tails of the two CMFs from the maps with noise are indistinguishable from that of the CMF of the map without noise. Essentially the same high-mass cores are selected (or at least the same CMF of high-mass cores), so thermal noise is not the main cause of the shift to larger masses of the high-mass tail of the CMF of synthetic ALMA cores, relative to that of the cores extracted from the column-density maps.

The second panel from the top of Fig. 12 proves that radiative transfer effects, given the grain model and the corresponding core temperature adopted here, have a small effect on the CMF. So an incorrect choice of temperature is not the cause of the larger masses of the synthetic ALMA cores relative to those from the column density maps. However, if we had assumed a dust opacity inconsistent with that of the grain model used in the radiative transfer calculations, or an incorrect dust temperature of the cores, we would have obtained a significant shift in mass relative to the cores from the column-density maps. Thus, in the analysis of real observational data, the choice of dust opacity and core temperature will generally cause significant systematic mass uncertainties. In addition, if an individual temperature is estimated for each core, significant random uncertainties are also introduced. These considerations about dust opacity and dust temperature are further discussed in Sections 7.3 and 7.5.

The middle panel of Fig. 12 shows that the main shift of the CMF towards larger masses occurs in the transition from the single-dish to the interferometric maps, where the same grain model and core temperature have been used. Thus, we can conclude that the high-mass tail of the synthetic ALMA CMF has an excess of massive cores relative to the CMF from the column-density maps, as well as a shallower slope, primarily due to interferometric artefacts (e.g. an increase of the luminosity contrast between the cores and their background). Because of the incomplete sampling of the (u,v) plane, interferometric images rely on interpolation whose weights are chosen based on assumptions about the source distribution. In the case of extended sources, one does not know a priori the real surface-brightness distribution, hence the incomplete (u,v) plane sampling and the interpolation process will always create artificial features in the final images, which are often referred to as interferometric artefacts (or interferometric noise).

Fig. 13 shows a comparison of GETSF core selections on a single-dish image without noise (upper panel) and the corresponding

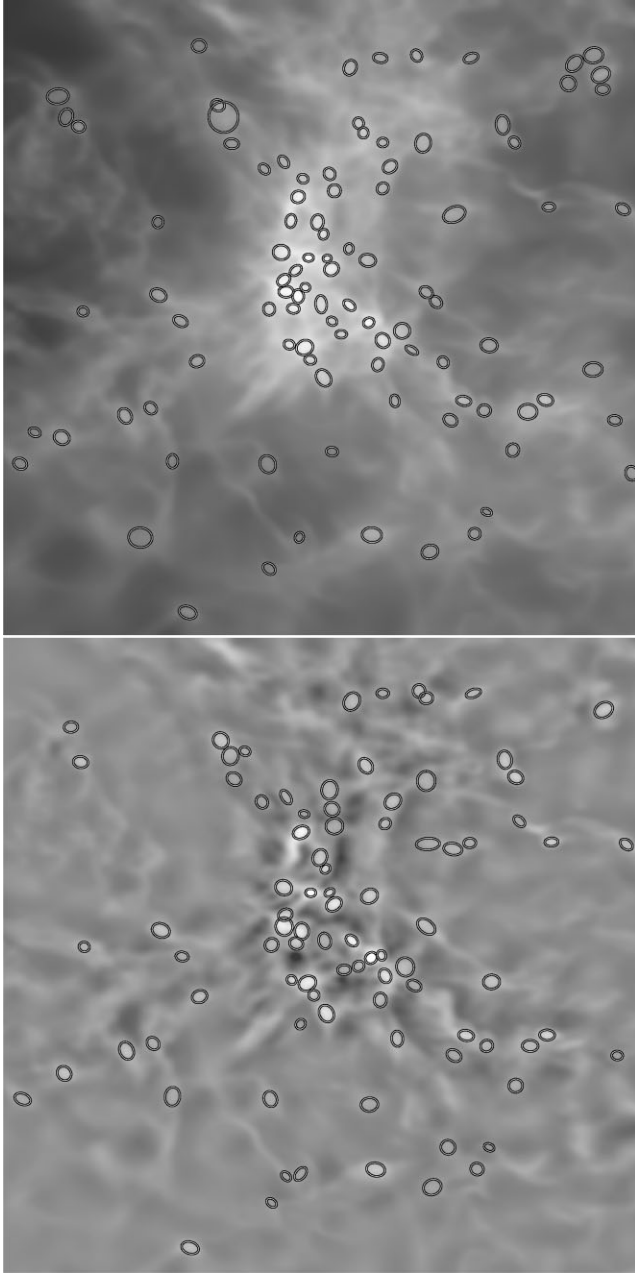


Figure 13. Examples of GETSF core selection on a single-dish image without noise (upper panel) and the corresponding synthetic ALMA map with the same beam size and also without noise (lower panel), corresponding to the panel 3,z of Fig. 1. The grey scale is proportional to the square root of the surface brightness in both panels, with minimum and maximum values set to 5.0 MJy sr⁻¹ (black colour) and 100.0 MJy sr⁻¹ (white colour) in both panels. The ellipses correspond to the FWHM of the cores extracted by GETSF.

synthetic ALMA map, also without thermal noise, with the same beam size (lower panel). Many cores in common between the two maps can be recognized, usually with comparable sizes. Yet, we know that the cores in the lower panel are on average approximately a factor of 2 more massive than the cores in the upper panel. Although a detailed explanation requires a careful examination of the various extraction steps in GETSF, it is clear that the background subtraction is affected by interferometric artefacts creating some artificial intensity contrasts in the ALMA maps, resulting in a slightly less aggressive

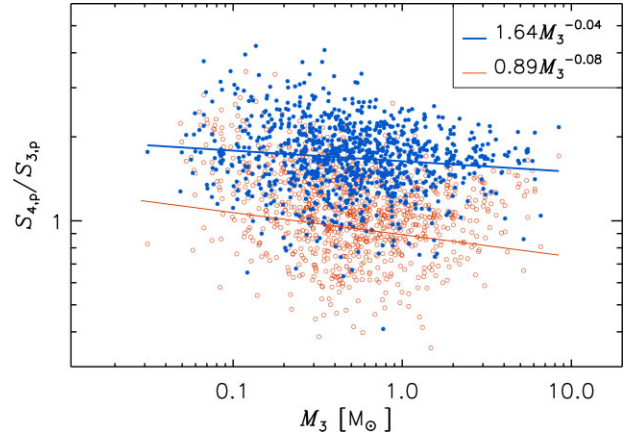


Figure 14. Ratio of peak surface brightness of GETSF cores selected from the simulated interferometric maps without noise, $S_{4,p}$, and from the simulated single-dish maps without noise, $S_{3,p}$. The blue filled circles are for the extracted GETSF values, which include the background subtraction, while the empty red circles are for the values without background subtraction.

subtraction. Because the background subtraction is often of order 90 per cent of the column density, a small difference in background subtraction from 90 per cent to 80 per cent, for example, would cause an increase in the extracted core mass by a factor of 2. This effect should be kept in mind, and possibly quantified, when assessing mass uncertainties of cores selected in interferometric surveys.

The scatter plots in Fig. 14 illustrate the effect of the background subtraction by comparing cores extracted from the single-dish maps with the corresponding cores extracted from the interferometric maps, both without noise. These are the same cores whose masses, M_3 and M_4 , respectively, are plotted in the middle panel of Fig. 12. The blue filled circles in Fig. 14 give the ratio between the peak surface brightness of the cores from the two types of maps, $S_{4,p}/S_{3,p}$, as a function of the mass of the cores from the single-dish maps, M_3 . The total scatter in the plot is approximately one order of magnitude, and the mean value of the peak-brightness ratio ~ 2 , consistent with the scatter and mean values of the mass ratio, M_4/M_3 , implied by the scatter plot in the middle panel of Fig. 12. However, the peak-brightness ratio without background subtraction is ~ 1 , as shown by the empty red circles in Fig. 14. This comparison of the two scatter plots, with and without background subtraction, confirms that the smaller background subtraction applied to the cores from the interferometric maps is the main reason for the shift of the CMF to larger masses, as discussed above.

7.3 The CMF in the W43 region

Pouteau et al. (2022) find that the high-mass tail of the CMF in the W43-MM2 and MM3 regions has a shallower slope than Salpeter's (as in the case of W43-MM1, previously studied by Motte et al. 2018b). This conclusion is based on plots of the cumulative CMF, which has the advantage of being independent of binning, but may also mask important features of the actual CMF. In the following comparison, we refer to the CMF, rather than its cumulative version. The comparison is independent of the uncertainty of the estimated core temperature, because all the core masses are derived from equation (1) using the same dust temperature value of $T_{\text{dust}} = 13.0$ K. Thus, we effectively compare the distributions of integrated 1.3 mm fluxes, rather than masses, even if the fluxes are expressed as masses. The mass conversion assumes $\kappa_{1.3\text{mm}} = 0.0037 \text{ cm}^2 \text{ g}^{-1}$

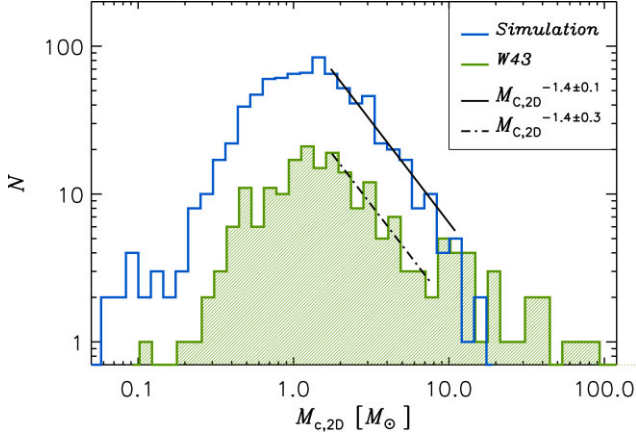


Figure 15. CMFs of GETSF cores selected from the synthetic ALMA maps (blue histogram) and of the W43-MM2 and MM3 cores from Pouteau et al. (2022) (green histogram) derived from the cores integrated fluxes and assuming a constant dust temperature (see the text for details). Power-law fits in the approximate mass interval 2–10 M_{\odot} are shown for both CMFs.

for our synthetic cores (consistent with our dust model and previous plots), and $\kappa_{1.3\text{mm}} = 0.01 \text{ cm}^2 \text{ g}^{-1}$ for the W43 cores, as assumed in Pouteau et al. (2022). This choice of T_{dust} and $\kappa_{1.3\text{mm}}$ results in a similar turnover mass for the CMF of W43 as for our synthetic cores. Using the median temperature estimated by Pouteau et al. (2022), $T_{\text{dust}} = 23 \text{ K}$, the CMF of W43 would shift to lower masses by a factor of 0.6, but both mass scaling probably underestimate the true masses of the W43 cores by a factor of 2 to 4, depending on the dust models (see Section 7.5).

The CMF from W43 (green histogram) and of our synthetic ALMA cores (blue histogram), computed with a single temperature as mentioned above, are shown in Fig. 15. In the limited range of masses between approximately 1.5 and 9 M_{\odot} , where the CMF of W43 may be approximated by a single power law, its slope is -1.4 ± 0.3 , consistent with that of our simulated regions. Both CMFs have a turnover at around 1.5 M_{\odot} , and a similar drop towards lower masses, but the value of the turnover for the CMF of W43 is entirely dependent on the choice of $\kappa_{1.3\text{mm}}$ and T_{dust} , and would be shifted to larger masses if a combination of values consistent with either of our dust models were used (see Section 7.5). The CMF of W43 shows a clear excess above approximately 9 M_{\odot} , where 25 cores are found, while only approximately 3 would be expected if the slope of -1.4 were to continue above 9 M_{\odot} .

7.4 Hypercritical pre-stellar cores, massive protostellar cores, or projection effects?

We can only speculate about the origin of the excess of cores above 9 M_{\odot} in the CMF of W43. To illustrate the special nature of these relatively massive cores, Fig. 16 shows the mass–size relation of our synthetic ALMA cores with blue empty circles, and of the cores in W43 with red filled circles. The W43 cores above 9 M_{\odot} are marked by larger red circles. The size, $D_{c,2D}$, is the beam-deconvolved FWHM, and the mass, $M_{c,2D}$, is derived in the same way as for the CMFs of Fig. 15. There is a significant overlap in the mass–size relation between our synthetic cores and those in W43, although the sizes of the synthetic cores are on average a factor of 2 larger. This is partly due to the fact that our beam size is slightly larger, 0.60 arcsec compared to 0.47 arcsec in W43 (see the dashed and dotted vertical lines in Fig. 16), partly a consequence of the limited resolution of the

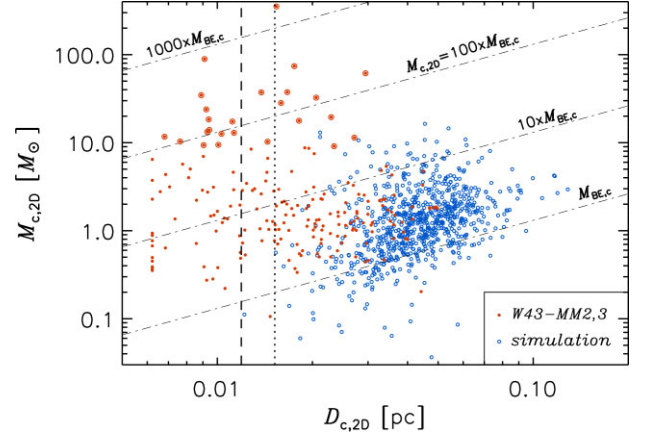


Figure 16. Mass–size relation for the synthetic ALMA cores (blue empty circles) from this work, and for the cores in the W43-MM2,MM3 region (red filled circles) from Pouteau et al. (2022). The size, $D_{c,2D}$, is the beam-deconvolved FWHM, and the mass, $M_{c,2D}$, is derived from the 1.3 mm flux assuming $T_{\text{dust}} = 13.0 \text{ K}$ (see the main text for details). The larger red circles mark the W43 cores more massive than 9 M_{\odot} . The diagonal dash–dotted lines correspond to constant values of $M_{c,2D}/M_{\text{BE},c}$, where $M_{\text{BE},c}$ is the critical Bonnor–Ebert mass for a temperature of 13.0 K. The vertical lines mark the beam sizes for the W43 observations (dashed line) and for the synthetic observations (dotted line).

simulation (a bit too close to the beam size). In addition, a significant fraction of the W43 cores have FWHM size close to the beam size, so many of them are further reduced in size after beam deconvolution. As a result, 28 per cent of the W43 cores have deconvolved sizes smaller than the beam size, while only one of the synthetic cores has a deconvolved size smaller than the beam size.

The diagonal dash–dotted lines represent constant values of the ratio $M_{c,2D}/M_{\text{BE},c}$, where $M_{\text{BE},c}$ is the critical Bonnor–Ebert mass (Bonnor 1956; Ebert 1957) for a temperature of 13.0 K. Considering only the cores with masses below 9 M_{\odot} , the median value of $M_{c,2D}/M_{\text{BE},c}$ is 2.1 for the synthetic cores, and 5.1 for the W43 cores, due to the smaller sizes of the latter. The only four synthetic cores above 9 M_{\odot} have a median $M_{c,2D}/M_{\text{BE},c}$ ratio of 20.5 (and a maximum value of 47.0), while the 25 cores in W43 have a median value of 118.6, with a maximum value of 1,747.⁶ Thus, the W43 cores responsible for the CMF excess at high masses are all *hypercritical*, as their $M_{c,2D}/M_{\text{BE},c}$ ratios are on average 50 times larger than those of the pre-stellar cores found in the simulation.

It seems unlikely that such hypercritical cores are pre-stellar in nature, as in MHD simulations with realistic magnetic-field strength gravitational collapse initiates as soon as cores grow to be a few times their critical Bonnor–Ebert mass (e.g. fig. 11 in Padoan et al. 2020). Their observed overabundance makes these cores even more unlikely to be pre-stellar, as the median density of the cores above 9 M_{\odot} in W43 is 43.0 times larger than that of the cores below 9 M_{\odot} , so their free-fall time is 6.6 times shorter, making them very short lived.⁷ Finally, if the core temperatures estimated in Pouteau et al. (2022) were correct for at least the most massive cores, they would

⁶If pairs of values of $\kappa_{1.3\text{mm}}$ and T_{dust} consistent with our dust models were used (see Section 7.5), the $M_{c,2D}/M_{\text{BE},c}$ ratios of the W43 cores would be even larger, by approximately a factor of 3.

⁷The median value of n_{H_2} of the W43 cores above 9 M_{\odot} is approximately $8 \times 10^7 \text{ cm}^{-3}$ (for the core mass contained within the FWHM size), which gives a free-fall time of only 3.4 kyr.

imply a protostellar nature, as dust temperatures in excess of 15 K are not expected at such high densities without internal heating sources with reasonable dust models (see Section 7.5 and references therein).

Thus, we speculate that, rather than being hypercritical pre-stellar cores, these objects are more likely to be protostellar cores. In that case, and given their small size, they may have already acquired a significant amount of rotation around the central star (depending on the magnetic-field strength and configuration), so they may be better described as pseudodiscs. Even if this interpretation were correct, such compact protostellar cores could not be present in our simulation, because the accretion radius of the sink particles is four times the minimum cell size, or 0.03 pc, so we cannot capture protostellar cores below a size of approximately 0.06 pc (this also explains the low temperature of our cores, as they are essentially all pre-stellar). Future observations of emission lines at comparable angular resolution may confirm the protostellar nature of the massive cores in W43 through the presence of outflows, if not by direct evidence of infall or of supersonic rotation of the cores. Simulations at higher resolution will also be needed.⁸

It is also possible that the mass estimate of a majority of the massive cores in W43 suffers from projection effects and limited resolution and sensitivity. Projection effects must be even stronger in W43 than in our simulation, due to the higher maximum column density and the greater observational depth (several kpc) through the Galactic plane in the inner Galaxy. Fig. 17 illustrates the difficulty of a 2D core extraction (upper panel) in a field with a large number of 3D cores (lower panel). The actual number of DENDRO cores is more than double of what is shown in the lower panel, as we only show the DENDRO cores with masses $> 0.5 M_{\odot}$ for clarity. One can see that, even if our simulated region does not reach the column density where the most massive W43 cores are found, there is a significant chance of overlap of 3D cores in the densest regions, so a single GETSF core may have contributions from several DENDRO cores. Thus, it is possible that the mass of some of the most massive cores in W43 is overestimated due to the overlap of multiple 3D cores along the line of sight. These projection effects – overlap of real 3D cores along the line of sight – should not be confused with the artefacts mentioned in Section 6, meaning 2D cores without a 3D counterpart. The case discussed here is quite the contrary: 2D cores with too many real 3D counterparts. However, if the most massive cores are protostellar, we cannot quantify the contribution of projection effects to their mass estimates, because protostellar cores are not captured by our simulation, as mentioned above.

Spatial resolution is also an important factor for compact-source extractions. When pre-stellar cores are selected as compact sources, they are not spatially resolved by definition. The largest ones, typically containing two to four beam sizes, have a measurable size, but their internal structure (e.g. the possibility of internal fragmentation) is unknown. Thus, cores extracted as compact sources should not be interpreted as individual objects in the absence of a strong physical justification for that assumption. The fact that cores extracted as compact sources are unresolved, in the sense that their sizes span a very limited range of values around the observational

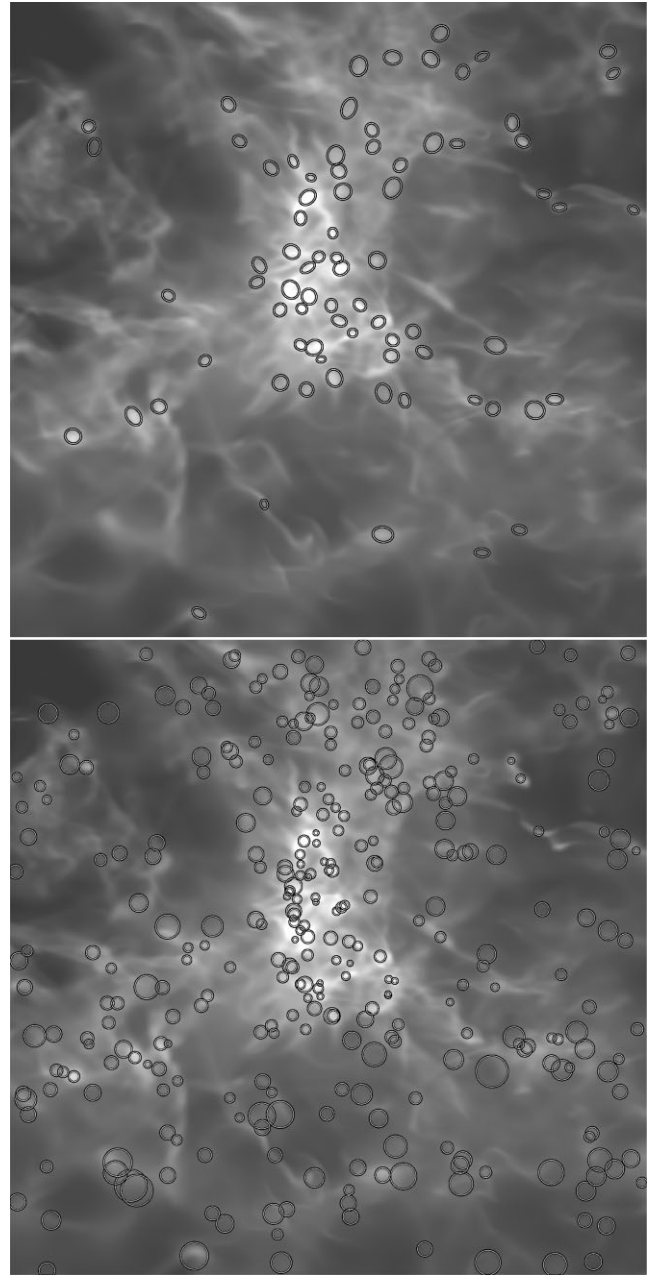


Figure 17. Comparison of 2D GETSF synthetic ALMA core positions (upper panel) with 3D DENDRO cores positions (lower panel) plotted over the same column-density image. The GETSF cores in the upper panel are the same as those in the lower panel of Fig. 4. The lower panel shows the position and the size of the DENDRO cores with masses $> 0.5 M_{\odot}$. The lower mass DENDRO cores are omitted for clarity.

⁸A new paper from the ALMA-IMF Large Program, Nony et al. (2023), which appeared after the submission of this work, confirms our prediction that most of the massive cores in W43, responsible for the shallower CMF at large masses, are in fact protostellar in nature (up to 80 per cent for masses above $16 M_{\odot}$). Excluding the protostellar cores, Nony et al. (2023) find that the CMF of W43 has a slope of $-1.46^{+0.12}_{-0.19}$, consistent with our value of -1.4 ± 0.1 for the CMFs of both W43 and our synthetic ALMA cores.

beam size, is well documented in the observational and numerical literature. Compact sources in the Hi-GAL Survey of the Galactic plane (Elia et al. 2021), extracted with the CUTEX code (Molinari et al. 2011), have sizes mostly below 2.5 times the (Herschel 250 μm) beam size (e.g. Molinari et al. 2016). In the W43 regions MM2 and MM3, Pouteau et al. (2022) find only five GETSF sources with sizes larger than four times the beam size, which they exclude from their analysis. Almost 90 per cent of their sources have a size below 3.0 times the beam size, similarly to the Hi-GAL sources. Based on synthetic Herschel observations and the same data-analysis pipeline

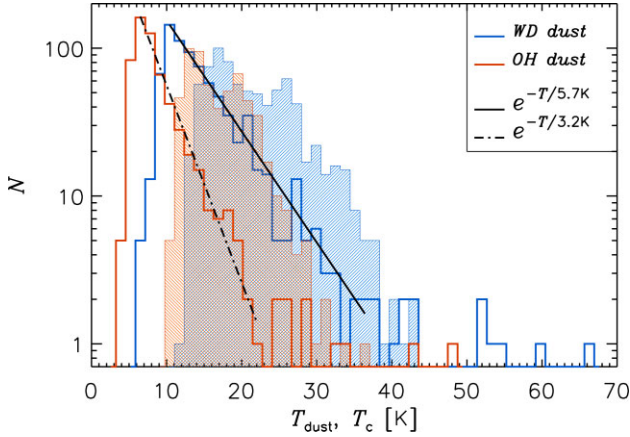


Figure 18. Distributions of the mass-weighted mean dust temperature, T_{dust} , of the candidate 3D cores (defined in Section 6.1.1) for the WD dust model (blue unshaded histogram) and the OH dust model (red unshaded histogram). The black solid and dash-dotted lines are the least-square fits reported in the legend. The shaded histograms are the distributions of the colour temperature, T_c , of the corresponding GETSF cores (see details in the main text) for the WD model (blue histogram) and the OH model (red histogram).

and source-extraction code as in the Hi-GAL survey, Lu et al. (2022) have shown that the Hi-GAL clumps are unresolved and their mass may not reflect at all that of the underlying cores (see their section 7.3 and fig. 15). Using both Herschel and ALMA synthetic observations, Padoan et al. (2020) have shown that core masses may be highly overestimated, for example, by a factor of 10 in the case of Herschel for regions at 1 kpc distance (see their section 9.2 and figures therein). They have also found that, even when the typical core masses are not overestimated on average, at the highest ALMA resolution, the estimated masses of individual cores show no correlation with the true core masses (see their fig. 27), in agreement with the results of this work (considering that interferometric artefacts were not included in Padoan et al. 2020). A more straightforward study of GETSF core extractions using column-density maps from simulations (with no radiative transfer or interferometric effects, analogous to Section 6.1.1 of this work) has demonstrated that the sizes of compact-sources depend on the beam size, hence the sources are unresolved and should not be interpreted as single objects, and beam deconvolution to extrapolate their size is not justified (Louvét et al. 2021).

7.5 Dust models and core temperature

All previous plots in this work are based on the Weingartner & Draine (2001) $R_V = 5.5$ dust model (Case B), with $\kappa_{1.3\text{ mm}} = 0.0037\text{ cm}^2\text{ g}^{-1}$. However, we have carried out the full analysis also with the dust model of Ossenkopf & Henning (1994), corresponding to dust that has evolved for 10^5 yr at a density of 10^6 cm^{-3} and has acquired thin ice mantles. This model has a significantly larger dust opacity, $\kappa_{1.3\text{ mm}} = 0.0083\text{ cm}^2\text{ g}^{-1}$. Although the conclusions of this work are not affected by the choice of the dust model, here we provide a brief comparison between the two cases, as well as a discussion of core temperatures. In the following text, we refer to the two dust models as the WD model and the OH model, respectively.

Fig. 18 shows the distribution of the dust temperature of the candidate 3D cores (see Section 6.1.1), computed as the mass-weighted mean temperature of the dust inside the spherical volume of each core. The unshaded blue histogram is for cores extracted

from the synthetic ALMA maps based on the WD model, while the unshaded red histogram from the maps computed with the OH model. As expected from the larger dust opacity, the OH model results in lower dust temperature at the high densities found in the cores. The median dust-temperature values, used to derive the core masses (see Section 5.1), are 13.0 K for the WD model and 7.5 K for the OH model. Both temperature distributions are very well approximated by exponential functions for dust temperatures above the peak (corresponding roughly to the median value), except for a few high-temperature outliers.

We also compute the colour temperature, T_c , of all the synthetic ALMA cores, using surface brightness maps at 100, 160, 250, 350, 500, 850, and 1300 μm . The wavelengths are similar to those used in Pouteau et al. (2022) (apart from the exclusion of the 70 μm band and the 870 μm wavelength being replaced with 850 μm). In the modified blackbody fits, we assume a constant dust opacity spectral index of $\beta = 1.8$ and the same relative uncertainty at all frequencies. The final colour temperature estimates are averages over the 2D footprint of each core. This method is less sophisticated than that used in Pouteau et al. (2022), which is based on the PPMAP method of Marsh, Whitworth & Lomax (2015), with some other corrections for the most massive cores and for cores with evidence of outflows. The PPMAP method is expected to result in a more accurate estimate for the mass-averaged dust temperatures than a straightforward colour temperature. However, our colour temperature is calculated on the precise footprint of each core, with all the bands computed at the full 0.60 arcsec resolution of our synthetic ALMA maps, while the PPMAP method yields a rather smooth temperature map at a nominal resolution of 2.5 arcsec. The distributions of T_c for all the synthetic ALMA cores are plotted in Fig. 18, where the shaded blue histogram is for the WD model, and the shaded red histogram for the OH model. The colour temperatures are clearly shifted to larger values than the dust temperatures of the candidate 3D cores, with median values of 20.4 and 16.0 K for the WD and OH models, respectively. The colour temperatures are higher because the pre-stellar cores are the coldest regions along the line of sight and because the colour temperature is most sensitive to the warmest regions that emit more strongly per unit mass.

Because the colour temperature can be estimated observationally, it is useful to derive an empirical relation between T_{dust} and T_c . Fig. 19 shows a scatter plot of T_{dust} versus T_c for our simulated cores (candidate 3D cores and corresponding GETSF cores, respectively), based on the WD dust model (empty blue circles) and on the OH model (filled red circles). The vertical scatter is quite large, particularly in the case of the OH model, but it is possible to fit linear relations in the log-log space, shown by the solid and dash-dotted lines in Fig. 19. For the WD model the relation is almost exactly linear, with the dust temperature typically 70 per cent of the colour temperature, $T_{\text{dust, WD}} = 7.2\text{ K} \times (T_{c, \text{WD}}/10\text{ K})^{0.91}$. For the OH model the fit is significantly shallower than linear, with the dust temperature typically 50 per cent of the colour temperature, $T_{\text{dust, OH}} = 5.6\text{ K} \times (T_{c, \text{OH}}/10\text{ K})^{0.72}$. These empirical relations hold for colour temperature maps at comparable angular resolution as the ALMA maps. This is not the case when combining for example the ALMA maps with Herschel images. In that case, since the colour temperature at larger scales has a greater contribution from the warmer background, the typical ratio between T_c and T_{dust} will be larger than reported here. Fig. 20 shows the case where T_c is computed from images at an angular resolution of 18 arcsec, corresponding to the 250 μm band of Herschel. As expected, the total range of T_c is decreased compared to the higher resolution case in Fig. 19. However, the mean relation between T_c and T_{dust} expressed

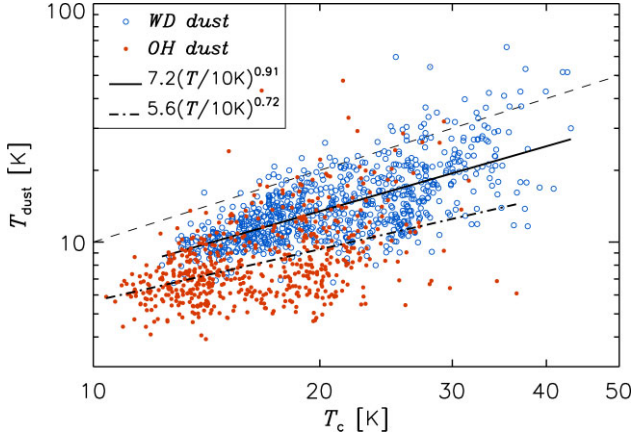


Figure 19. Dust temperature (of the candidate 3D cores) versus colour temperature (of the corresponding GETSF cores) from the WD dust model (blue empty circles) and the OH dust model (filled red circles). The black solid and dash–dotted lines are the linear fits reported in the legend, and the thin dashed line is the one-to-one relation.

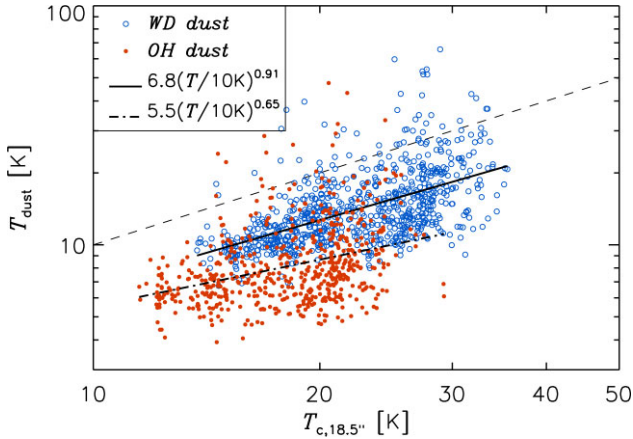


Figure 20. The same as Fig. 19, but with T_c computed at an angular resolution of 18 arcsec.

by the linear fit barely changes in the case of the WD dust model,

$$T_{\text{dust,WD}} = 6.8 \text{ K} \times (T_{c,\text{WD}}/10 \text{ K})^{0.91}. \quad (2)$$

The change is instead significant for the OH model,

$$T_{\text{dust,OH}} = 5.5 \text{ K} \times (T_{c,\text{OH}}/10 \text{ K})^{0.65}, \quad (3)$$

due to the larger temperature variations as a function of density caused by the higher opacity relative to the WD model, which is further discussed below. Equations (2) and (3) may be used to convert estimated colour temperature maps from Herschel observations into dust temperatures of cores extracted from ALMA observations, though the conversion should be derived again for different ALMA angular resolution or different distance of the observed region.

Fig. 21 compares the CMFs of the synthetic ALMA cores extracted from the maps computed with the WD model (blue unshaded histogram) and with the OH model (red unshaded histogram). The core masses are derived from the integrated GETSF 1.3 mm fluxes, using equation (1), the $\kappa_{1.3 \text{ mm}}$ value of each model, and the median dust temperature of the candidate 3D cores as explained in Section 5.1, $T_{\text{dust}} = 13.0 \text{ K}$ and 7.5 K for the WD and OH models, respectively. The CMF based on the OH model is clearly shifted towards lower

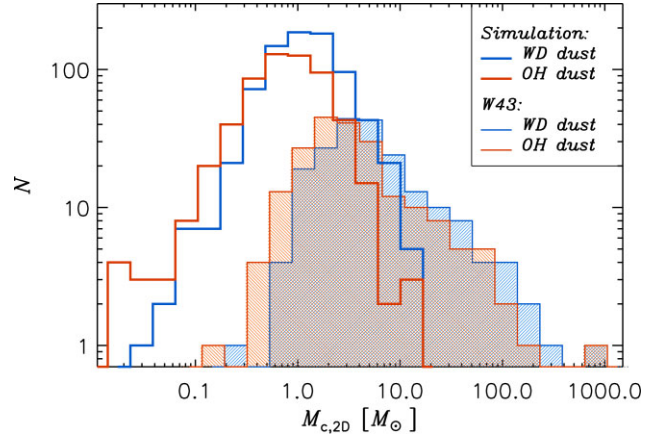


Figure 21. CMFs of the synthetic ALMA cores (unshaded histograms) from radiative transfer calculations with the WD dust model (blue histogram) and the OH dust model (red histogram). The shaded histograms are the CMFs of the W43 cores with masses derived from the integrated 1.3 mm fluxes in Pouteau et al. (2022) using the optically thin approximation of equation (1) with $T_{\text{dust}} = 14.4 \text{ K}$ and $\kappa_{1.3 \text{ mm}} = 0.0037 \text{ g cm}^{-2}$, as in the case of the WD dust model (blue histogram), and with $T_{\text{dust}} = 9.8 \text{ K}$ and $\kappa_{1.3 \text{ mm}} = 0.0083 \text{ g cm}^{-2}$, as in the case of the OH dust model (red histogram). The histograms of the W43 cores have been shifted to the right by a factor of 1.1 for clarity.

masses, by nearly a factor of 2, relative to the CMF from the WD model. This shift can be understood as the effect of the higher opacity of the OH model, resulting in higher temperatures in the diffuse medium and lower in dense cores in comparison to the WD model. The stronger dependence of the dust temperature on density in the OH model causes a stronger background subtraction, hence a lower core mass estimate, than in the WD model. This is related to the rim-brightening effects discussed in Men'shchikov (2016, see Section 5.2 and Appendix B). Other sources of uncertainties in the conversion of integrated fluxes to masses, due to spatial variations in temperature and dust-opacity, have been discussed in the literature (e.g. Malinen et al. 2011; Roy et al. 2014; Pagani et al. 2015; Men'shchikov 2016).

The radiative transfer calculations result in self-consistent dust temperature and opacity values, depending on the adopted dust model. Given that both are quite difficult to establish observationally, one may interpret the observations based on the temperature and opacity values from the simulation. This is shown in Fig. 21, where the shaded histograms are the CMFs of the MM2 and MM3 regions of W43 derived from the integrated 1.3 mm fluxes in Pouteau et al. (2022), and the core masses are computed with the same pairs of values of $\kappa_{1.3 \text{ mm}}$ and T_{dust} of the two dust models as in the case of the synthetic CMFs. The blue shaded histogram is based on the WD model, and the red shaded histogram on the OH model. The OH model causes a similar shift to lower masses relative to the WD model as in the case of the synthetic CMFs, but in this case the shift has a trivial origin, because the two CMFs are based on the same core extraction (the same integrated 1.3 mm fluxes): the ratio of the two opacities is larger than the ratio of the two median temperatures, so the larger opacity OH model results in lower masses.

Besides the trivial dependence of the W43 CMF on the dust models, the more important result is the significant shift of the CMF to larger masses relative to the synthetic CMF and to the CMF in Pouteau et al. (2022), where typical dust temperatures in excess of 20 K are derived, while assuming a high dust opacity, $\kappa_{1.3 \text{ mm}} = 0.01 \text{ cm}^2 \text{ g}^{-1}$. Based on our simulation and radiative-

transfer calculations, and assuming that the cores are mostly pre-stellar as in our case, hence externally heated, such opacity value should yield rather low temperatures and hence larger masses than in Pouteau et al. (2022). Temperatures below 10 K and even down to 6 K have been observed in low-mass pre-stellar cores, based on spectral line observations of regions where the gas and dust temperatures should be closely coupled (Crapsi et al. 2007; Harju et al. 2008). Similarly low temperatures have been found in radiative transfer models, where (depending on the dust properties) the dust temperatures fall below 10 K already in regions that are shielded by less than $A_V = 10$ mag of extinction (Zucconi, Walmsley & Galli 2001; Stamatellos, Whitworth & Ward-Thompson 2007; Chacón-Tanarro et al. 2019). Alternatively, if most of the W43 cores were protostellar, internal heating from the protostars may cause higher dust temperatures closer to those estimated in Pouteau et al. (2022), but then the implications of the derived CMF for the origin of the stellar IMF would no longer be relevant.

8 CONCLUSIONS

We have identified and studied 12 regions forming high-mass stars in our 250 pc star formation simulation, driven self-consistently by SNe for over 40 Myr. We have generated synthetic ALMA 1.3 mm maps of these regions, by solving the radiative transfer with thousands of point sources, including all stars with mass $> 2 M_\odot$ formed self-consistently in the simulation. The synthetic ALMA images have been processed by following the same analysis pipeline and source-extraction code as in the ALMA-IMF Large Program. The cores extracted from the synthetic images with the GETSF code have been compared with a sample of cores extracted independently with the DENDRO code from the $2 \text{ pc} \times 2 \text{ pc} \times 250 \text{ pc}$ volumes used to generate the maps. The comparison shows that the masses of the cores from the synthetic maps are only very weakly correlated to those of the corresponding 3D cores, while the shapes and slopes of the CMFs remain roughly similar, despite the fact that the CMF from the synthetic maps is incomplete at all masses relative to the CMF from the corresponding 3D volumes.

By first analysing column-density maps, we have studied the role of projection effects while excluding other effects from radiative transfer, interferometer artefacts, and thermal noise. The analysis shows that a significant fraction of the 2D GETSF cores are projection artefacts, an even larger fraction of 3D DENDRO cores are not retrieved in 2D, and the ones that are retrieved in 2D have estimated masses with large uncertainties. The following is a list of our main conclusions with respect to the core detection from column-density maps at a resolution of $\sim 0.01 \text{ pc}$, comparable to that of the ALMA-IMF project:

- (i) The mass of the 2D GETSF cores is strongly correlated with the mass of the main density structure in their line of sight, showing that the background subtraction of GETSF works well in column-density maps despite the complex density field, although the extracted cores may not be real cores in 3D.
- (ii) The fraction of projection artefacts, 2D GETSF cores without a 3D DENDRO counterpart, is a nearly monotonic function of mass, growing with decreasing mass from approximately 5 per cent above $2 M_\odot$ to over 50 per cent below $0.1 M_\odot$.
- (iii) The completeness fraction, 3D DENDRO cores with a 2D GETSF counterpart, increases monotonically with increasing mass without reaching unity. Above $1 M_\odot$, approximately 40 per cent of the 3D-selected cores are recovered in 2D.

(iv) The mass of the 2D GETSF cores is only a rough estimate of that of the associated 3D cores, with an uncertainty of approximately a factor of 4, and a tendency to increasingly underestimate the 3D core mass towards increasing masses.

(v) The slope of the 2D CMF above $1 M_\odot$ is -1.6 ± 0.1 , steeper than that of the 3D CMF, -1.2 ± 0.1 .

When including effects from radiative transfer, interferometric artefacts, and thermal noise using the synthetic 1.3 mm ALMA maps, the ability to retrieve the correct core masses worsens significantly compared to the idealized case of the column-density maps. Our main conclusions with respect to the selection of cores in the synthetic ALMA maps, with comparable resolution and the same image processing and analysis as in the ALMA-IMF Large Program, are listed in the following text:

(i) Overall, 70 per cent of the synthetic ALMA cores have a 3D counterpart. Above $3 M_\odot$ only 10 per cent of them can be considered projection artefacts.

(ii) A rather small fraction of the 3D DENDRO cores are detected as GETSF cores in the synthetic ALMA maps. The completeness fraction decreases monotonically with decreasing mass at all masses, from 40 per cent at $10 M_\odot$ to 15 per cent at $1 M_\odot$.

(iii) When a 3D counterpart is found, there is only a *weak correlation* between the masses of the synthetic ALMA cores and those of the corresponding 3D cores. Interferometric artefacts, radiative transfer effects, and thermal noise cause a significant increase in the random error of the estimated core masses, relative to the idealized case of the column-density maps.

(iv) The slope of the CMF of the synthetic ALMA cores above $1 M_\odot$, -1.4 ± 0.1 , is shallower than that of the cores selected from the column-density maps at the same spatial resolution, -1.6 ± 0.1 (while still steeper than that of the 3D CMF, -1.2 ± 0.1). This is primarily due to the combined effects of radiative transfer (spatial variations of the dust temperature) and interferometric artefacts (incomplete sampling of the (u,v) plane).

(v) Interferometric artefacts are found to cause a systematic shift in the derived masses of the synthetic ALMA cores, relative to those of the 2D GETSF cores from the column-density maps. A systematic shift of a similar magnitude is also caused by the choice of different dust models.

(vi) The colour temperature overestimates the real dust temperature in the cores. Empirical relations are derived to convert colour temperatures from Herschel observations into dust temperature of cores extracted from ALMA observations.

Guided by the results of this analysis, we conclude that core masses and CMFs from current ALMA observations of Galactic protoclusters at kpc distances should not be taken at face value. With the combined use of observations and realistic simulations, it should eventually be possible to set strong constraints on the CMF, but it seems pre-mature at this stage to draw conclusions on the origin of the stellar IMF directly from the observational results. We have shown that the observed CMF is expected to be a bit steeper than that of the real 3D cores, for the specific observational strategy, data-analysis pipeline, and source distances of the ALMA-IMF Large Program, and for star-forming regions like those found in our simulation. A general calibration of the relation between the real and observed CMFs will require a systematic study of the effects of spatial resolution and (u, v) plane sampling and interpolation methods, as well as a set of simulated star-forming regions covering a wide range of physical conditions.

ACKNOWLEDGEMENTS

Use of GETSF, developed by Alexander Men'shchikov at the DAP, IRFU, CEA Saclay, France, is hereby acknowledged. We also thank Alexander Men'shchikov for his guidance in the use of GETSF. We are grateful to Timea Csengeri for providing an updated version of the table 4 in Csengeri et al. (2017) used to produce our Fig. 2, and to Yohan Pouteau and Frédérique Motte for clarifications of some aspects of the ALMA-IMF Large Program data-analysis pipeline. Several comments by the referee and by members of the ALMA-IMF Large Program have helped us improve the paper. PP and VMP acknowledge financial support by the grant PID2020-115892GB-I00, funded by MCIN/AEI/ 10.13039/501100011033 and by the grant CEX2019-000918-M funded by MCIN/AEI/ 10.13039/501100011033. MJ acknowledges support from the Academy of Finland grant No. 348342. The research leading to these results has received funding from the Independent Research Fund Denmark through grant No. DFF 8021-00350B (TH). We acknowledge PRACE for awarding us access to Joliot-Curie at GENCI@CEA, France. The astrophysics HPC facility at the University of Copenhagen, supported by research grants from the Carlsberg, Novo, and Villum foundations, was used for carrying out the post-processing, analysis, and long-term storage of the results.

DATA AVAILABILITY

Supplemental material can be obtained from a dedicated public URL (<http://www.erd.dk/vgrid/alma-imf/>).

REFERENCES

- Alves J., Lombardi M., Lada C. J., 2007, *A&A*, 462, L17
- André P. et al., 2010, *A&A*, 518, L102
- Bonnell I. A., Bate M. R., Clarke C. J., Pringle J. E., 2001a, *MNRAS*, 323, 785
- Bonnell I. A., Clarke C. J., Bate M. R., Pringle J. E., 2001b, *MNRAS*, 324, 573
- Bonnor W. B., 1956, *MNRAS*, 116, 351
- Cao Y., Qiu K., Zhang Q., Wang Y., Xiao Y., 2021, *ApJ*, 918, L4
- Chabrier G., 2005, in Corbelli E., Palla F., Zinnecker H. eds, *Astrophysics and Space Science Library*, Vol. 327, *The Initial Mass Function 50 Years Later*. Springer-Verlag, Berlin, p. 41
- Chacón-Tanarro A. et al., 2019, *A&A*, 623, A118
- Compiègne M. et al., 2011, *A&A*, 525, A103
- Crapsi A., Caselli P., Walmsley M. C., Tafalla M., 2007, *A&A*, 470, 221
- Csengeri T., Bontemps S., Wyrowski F., Megeath S. T., Motte F., Sanna A., Wienen M., Menten K. M., 2017, *A&A*, 601, A60
- Dunham M. K., Rosolowsky E., Evans Neal J. I., Cyganowski C., Urquhart J. S., 2011, *ApJ*, 741, 110
- Ebert R., 1957, *Z. Astrophys.*, 42, 263
- Elia D. et al., 2021, *MNRAS*, 504, 2742
- Enoch M. L., Glenn J., Evans II N. J., Sargent A. I., Young K. E., Huard T. L., 2007, *ApJ*, 666, 982
- Fromang S., Hennebelle P., Teyssier R., 2006, *A&A*, 457, 371
- Ginsburg A. et al., 2022, *A&A*, 662, A9
- Gnedin N. Y., Hollon N., 2012, *ApJS*, 202, 13
- Habing H. J., 1968, *Bull. Astron. Inst. Neth.*, 19, 421
- Harju J., Juvela M., Schlemmer S., Haikala L. K., Lehtinen K., Mattila K., 2008, *A&A*, 482, 535
- Haugbølle T., Padoan P., Nordlund Å., 2018, *ApJ*, 854, 35
- Heiles C., Troland T. H., 2005, *ApJ*, 624, 773
- Hennebelle P., Chabrier G., 2008, *ApJ*, 684, 395
- Heyer M. H., Brunt C. M., 2004, *ApJ*, 615, L45
- Hildebrand R. H., Whitcomb S. E., Winston R., Stiening R. F., Harper D. A., Moseley S. H., 1977, *ApJ*, 216, 698
- Hopkins P. F., 2012, *MNRAS*, 423, 2037
- Juvela M., 2019, *A&A*, 622, A79
- Kauffmann J., Pillai T., 2010, *ApJ*, 723, L7
- Kong S., 2019, *ApJ*, 873, 31
- Könyves V. et al., 2010, *A&A*, 518, L106
- Könyves V. et al., 2015, *A&A*, 584, A91
- Könyves V. et al., 2020, *A&A*, 635, A34
- Kroupa P., 2001, *MNRAS*, 322, 231
- Kumar M. S. N., Palmeirim P., Arzoumanian D., Inutsuka S. I., 2020, *A&A*, 642, A87
- Kumar M. S. N., Arzoumanian D., Men'shchikov A., Palmeirim P., Matsumura M., Inutsuka S., 2022, *A&A*, 658, A114
- Ladjelate B. et al., 2020, *A&A*, 638, A74
- Larson R. B., 1981, *MNRAS*, 194, 809
- Li S., Zhang Q., Pillai T., Stephens I. W., Wang J., Li F., 2019, *ApJ*, 886, 130
- Louvet F., Hennebelle P., Men'shchikov A., Didelon P., Ntormousi E., Motte F., 2021, *A&A*, 653, A157
- Lu Z.-J., Pelkonen V.-M., Padoan P., Pan L., Haugbølle T., Nordlund Å., 2020, *ApJ*, 904, 58
- Lu Z.-J., Pelkonen V.-M., Juvela M., Padoan P., Haugbølle T., Nordlund Å., 2022, *MNRAS*, 510, 1697
- Malinen J., Juvela M., Collins D. C., Lunttila T., Padoan P., 2011, *A&A*, 530, A101
- Marsh K. A., Whitworth A. P., Lomax O., 2015, *MNRAS*, 454, 4282
- Marsh K. A. et al., 2016, *MNRAS*, 459, 342
- Mathis J. S., Mezger P. G., Panagia N., 1983, *A&A*, 128, 212
- McKee C. F., Tan J. C., 2002, *Nature*, 416, 59
- McKee C. F., Tan J. C., 2003, *ApJ*, 585, 850
- Men'shchikov A., 2016, *A&A*, 593, A71
- Men'shchikov A., 2021a, *A&A*, 649, A89
- Men'shchikov A., 2021b, *A&A*, 654, A78
- Molinari S., Schisano E., Faustini F., Pestalozzi M., di Giorgio A. M., Liu S., 2011, *A&A*, 530, A133
- Molinari S. et al., 2016, *A&A*, 591, A149
- Motte F., Andre P., Neri R., 1998, *A&A*, 336, 150
- Motte F. et al., 2018a, *Nat. Astron.*, 2, 478
- Motte F., Bontemps S., Louvet F., 2018b, *ARA&A*, 56, 41
- Motte F. et al., 2022, *A&A*, 662, A8
- Myers P. C., 2009, *ApJ*, 700, 1609
- Nony T. et al., 2023, preprint ([arXiv:2301.07238](https://arxiv.org/abs/2301.07238))
- Nutter D., Ward-Thompson D., 2007, *MNRAS*, 374, 1413
- Ossenkopf V., Henning T., 1994, *A&A*, 291, 943
- Padoan P., Nordlund Å., 2002, *ApJ*, 576, 870
- Padoan P., Nordlund Å., 2011, *ApJ*, 741, L22
- Padoan P., Nordlund Å., Kritsuk A. G., Norman M. L., Li P. S., 2007, *ApJ*, 661, 972
- Padoan P., Haugbølle T., Nordlund Å., 2014, *ApJ*, 797, 32
- Padoan P., Pan L., Haugbølle T., Nordlund Å., 2016a, *ApJ*, 822, 11
- Padoan P., Juvela M., Pan L., Haugbølle T., Nordlund Å., 2016b, *ApJ*, 826, 140
- Padoan P., Haugbølle T., Nordlund Å., Frimann S., 2017, *ApJ*, 840, 48
- Padoan P., Pan L., Juvela M., Haugbølle T., Nordlund Å., 2020, *ApJ*, 900, 82
- Pagani L., Lefèvre C., Juvela M., Pelkonen V. M., Schuller F., 2015, *A&A*, 574, L5
- Pan L., Padoan P., Haugbølle T., Nordlund Å., 2016, *ApJ*, 825, 30
- Pelkonen V. M., Padoan P., Haugbølle T., Nordlund Å., 2021, *MNRAS*, 504, 1219
- Peretto N. et al., 2014, *A&A*, 561, A83
- Pillai T., Kauffmann J., Zhang Q., Sanhueza P., Leurini S., Wang K., Sridharan T. K., König C., 2019, *A&A*, 622, A54
- Pouteau Y. et al., 2022, *A&A*, 664, A26
- Robitaille J. F., Motte F., Schneider N., Elia D., Bontemps S., 2019, *A&A*, 628, A33
- Rosolowsky E. W., Pineda J. E., Kauffmann J., Goodman A. A., 2008, *ApJ*, 679, 1338
- Roy A. et al., 2014, *A&A*, 562, A138
- Salpeter E. E., 1955, *ApJ*, 121, 161

- Sanhueza P., Jackson J. M., Zhang Q., Guzmán A. E., Lu X., Stephens I. W., Wang K., Tatematsu K., 2017, *ApJ*, 841, 97
- Sanhueza P. et al., 2019, *ApJ*, 886, 102
- Schaller G., Schaerer D., Meynet G., Maeder A., 1992, *A&AS*, 96, 269
- Schneider N. et al., 2012, *A&A*, 540, L11
- Servajean E., Garay G., Rathborne J., Contreras Y., Gomez L., 2019, *ApJ*, 878, 146
- Sokol A. D. et al., 2019, *MNRAS*, 483, 407
- Stamatellos D., Whitworth A. P., Ward-Thompson D., 2007, *MNRAS*, 379, 1390
- Takemura H. et al., 2021, *ApJ*, 910, L6
- Takemura H. et al., 2023, *ApJS*, 264, 35
- Teyssier R., 2002, *A&A*, 385, 337
- Teyssier R., 2007, *Geophys. Astrophys. Fluid Dyn.*, 101, 199
- Tigé J. et al., 2017, *A&A*, 602, A77
- Weingartner J. C., Draine B. T., 2001, *ApJ*, 548, 296
- Wolfire M. G., Hollenbach D., McKee C. F., Tielens A. G. G. M., Bakes E. L. O., 1995, *ApJ*, 443, 152
- Zhou J.-W. et al., 2023, *MNRAS*, 519, 2391
- Zinnecker H., 1982, *Ann. New York Acad. Sci.*, 395, 226
- Zucconi A., Walmsley C. M., Galli D., 2001, *A&A*, 376, 650

This paper has been typeset from a \LaTeX file prepared by the author.